National Technical University of Athens
School of Mechanical Engineering
Fluids Section

Application of the parabolic equation on the simulation of sound propagation in the atmospheric environment over complex terrain

Diploma Thesis

Athanasios Plevritis

Supervisor:

Vasilis A. Riziotis (Associate Professor)

Co - supervisor:

John M. Prospathopoulos (Teaching and Research Associate)

Athens, July 2023

Acknowledgements

This thesis marks the end of my undergraduate studies. I would like to express my gratitude to all those who contributed to this work.

First and foremost, I express my deepest thanks to Dr. John M. Prospathopoulos for giving me the opportunity to conduct my diploma thesis on such an interesting subject. I thank him for being available to discuss the progress of my work and providing me with valuable insights. Without his unique guidance, support, and encouragement, this endeavor would not have been possible.

I would also want to thank Associate Professor Vasilis A. Riziotis for providing me with an enriching academic environment to work in. The commitment and passion that he brought into his lectures had a profound impact on my academic growth.

Special thanks go to PhD candidate Dimitris Vlastos who provided assistance and expertise in specific areas of this thesis.

Finally, I would like to thank my family for believing in me from the start and supporting me throughout this academic journey.

Abstract

Noise pollution is an increasingly significant issue with detrimental effects on both biodiversity and human health. Transportation systems, construction sites and industrial machinery are some pertinent examples that contribute to excessive noise levels. To address these issues, there is a growing need for environmentally friendly designs in noise-generating facilities that aim to mitigate the harmful effects of noise pollution on human well-being and the natural environment. The current study incorporates the effects of irregular terrain and atmospheric turbulence in sound propagation. A fast Generalized Terrain Parabolic Equation (GTPE) model is developed, which utilizes a grid transformation that creates a fitted computational mesh for any terrain geometry that does not exceed the inclination limit of 30°. Also, this model incorporates atmospheric turbulence using the refractive-index fluctuation function, which introduced into the solution the temperature and wind velocity fluctuations that characterize the turbulent atmosphere. The developed GTPE model is applied on sound propagation over hills in non-turbulent atmosphere, and the comparison shows good agreement with the results of other models. The effect of a more realistic flow field, obtained from the solution of Navier-Stokes equations, is assessed. Application on sound propagation in turbulent atmosphere over flat terrain exhibits good agreement against measurements and predictions of other models.

Περίληψη

Η ηχορύπανση αποτελεί έναν ολοένα και πιο σημαντικό ζήτημα με επιβλαβείς επιπτώσεις τόσο στη βιοποικιλότητα όσο και στην ανθρώπινη υγεία. Μέσα μεταφοράς, οικοδομικές εργασίες και βιομηχανικά μηχανήματα είναι μερικά χαρακτηριστικά παραδείγματα που συνεισφέρουν στη παραγωγή επικίνδυνων επιπέδων θορύβου. Για να αντιμετωπιστούν αυτές οι προκλήσεις υπάρχει αυξανόμενη ανάγκη για το σχεδιασμό των εγκαταστάσεων που παράγουν θόρυβο με τρόπους φιλικούς προς το περιβάλλον, έτσι ώστε να μειωθούν οι επιβλαβείς επιπτώσεις της ηχορύπανσης . Στη παρούσα μελέτη εξετάζονται οι επιδράσεις της σύνθετης τοπογραφίας και της ατμοσφαιρικής τύρβης στη διάδοση του ήχου. Αναπτύσσεται ένα μοντέλο που βασίζεται στη Γενικευμένη Παραβολική Εξίσωση Εδάφους (GTPE), το οποίο χρησιμοποιεί ένα καμπυλόγραμμο υπολογιστικό πλέγμα το οποίο ακολουθεί τη γεωμετρία του εδάφους, υπό την προϋπόθεση ότι η κλίση του εδάφους δεν υπερβαίνει τις 30°. Επίσης, το μοντέλο αυτό ενσωματώνει την ατμοσφαιρική τύρβη εισάγοντας τις διακυμάνσεις του δείκτη διάθλασης, ο οποίος καθορίζεται μέσω των διαταραχών της θερμοκρασίας και της ταχύτητας του ανέμου που χαρακτηρίζουν την ατμοσφαιρική τύρβη. Το μοντέλο GTPE εφαρμόζεται σε περιπτώσεις διάδοσης του ήχου πάνω από λόφους σε μη τυρβώδες περιβάλλον και έρχεται σε καλή συμφωνία με τα αποτελέσματα άλλων μοντέλων. Επιπλέον, αξιολογείται η χρήση ενός ακριβέστερου πεδίου ροής το οποίο λαμβάνεται από την επίλυση των εξισώσεων Navier-Stokes. Η εφαρμογή του μοντέλου στη διάδοση του ήχου σε τυρβώδη ατμόσφαιρα πάνω από επίπεδη τοπογραφία δίνει αποτελέσματα που έρχονται σε καλή συμφωνία τόσο με μετρήσεις όσο και με προλέξεις άλλων μοντέλων.

Contents

1. Introduction

1.1 Technological problem and environmental needs

Noise pollution is gaining growing significance as the effects of anthropogenic noise on biodiversity but also on human health are becoming progressively more obvious. Transportation systems, including road traffic, aviation and railways [1] but also construction sites, industrial machines and domestic appliances constitute major contributors to noise pollution. Furthermore, recreational activities like concerts and sport events combined with poor urban planning amplify the acoustic burden on individuals and communities.

It is estimated that across Europe 113 million people are affected by noise levels that exceed 55 decibels, the limit at which noise levels can become harmful to humans [2]. The detrimental effects of noise pollution on human health have been extensively documented. Extended exposure to increased noise levels can lead to a range of health and behavior issues. These include both auditory and non-auditory health effects. Some pertinent examples are cardiovascular disorders, hearing loss and sleeping disturbances [3].

The ecological consequences of noise pollution extend beyond human health and pose significant threats to wildlife and ecosystems. This disturbance interferes with the crucial acoustic communication channels necessary for reproductive behaviors and territory defense [4] but also disturbs the ecological balance within ecosystems. Consequently, these disturbances contribute to gradual decline in biodiversity and thus mitigation measures are needed with the scope of protecting wildlife populations and their habitats.

As the harmful effects of noise pollution become more evident, the need for more environmentally friendly designs of noise generating facilities (airports, urban planning, railways etc.) arises. In real world scenarios the terrain and elevation of the area surrounding the noise source can be complex, including hills and valleys. An effective method to reduce noise level is to predict it before a new installation begins operating. To achieve this, certain tasks need to be undertaken: a) Estimating the amount of sound power generated by the noise sources, and b) Simulating how the sound will propagate in the atmospheric environment. The present work deals with the problem of noise propagation when the spectrum of the sound power level of the source is known.

1.2 Literature review

Over the past few decades, various computational methods have been created to simulate the propagation of atmospheric noise. These methods include the Parabolic Equation, Ray Theory, Fast Field Program (FFP), Normal Modes and Linearized Euler Equations by use of finite differences or finite volumes. A concise explanation of the principles and developed models of each method is presented below, along with the selected method used in this study.

Ray theory is built upon the assumption that sound travels along rays that are perpendicular to wave fronts, which are the surfaces representing constant phase of acoustic waves. The computational approach called ray tracing is employed to compute the paths or trajectories followed by these rays originating from a sound source. Ray theory is derived from the wave equation by introducing certain simplifications and is primarily used as a high-frequency approximation method [5].

The rays originating from the sound source and reaching the receiver are referred to as "eigenrays." The contribution of each eigenray to the overall sound pressure level is computed by subtracting the losses experienced along the trajectory from the source's sound power level. This calculation provides the amplitude of the complex pressure field, while the phase is estimated based on the integration time along the eigenray. The total sound pressure field perceived by the receiver is then determined by combining the contributions from all the eigenrays [6].

One significant limitation of the ray theory is its tendency to underestimate the sound pressure level during upwind sound propagation. This is attributed to the occurrence of "shadow zones" where the pressure field is calculated as zero [7]. In reality, the diffraction of sound around obstacles can contribute to the sound pressure level. Although these drawbacks permit ray theory from predicting accurately sound pressure levels, modern approaches where ground and atmospheric absorption, wave refraction and diffraction and atmospheric turbulence are considered show significant agreement with measurements [8].

The Fast Field Program (FFP) method, initially developed by Pekeris [9] for underwater acoustics, was first employed for atmospheric sound propagation by Lee et al. [10], specifically for scenarios involving complex impedance ground. This method is based on the principle of performing a Fourier transformation of the wave equation. This transformation involves converting the equation from the spatial domain to the horizontal wave number domain. The resulting transformed wave equation is then solved numerically, and the solution is transformed back to the spatial domain using an inverse Fourier transformation. Consequently, the solution in the spatial domain can be represented as an inverse Fourier integral over horizontal wave numbers. This characteristic has led to the FFP method being referred to as the "wave number integration method" [11].

As a consequence of the Fourier transformation to the horizontal wave number domain, the FFP method is restricted to systems with a layered atmosphere and a homogeneous ground surface. In other words, the FFP method is not suitable for accurately simulating systems with a range-dependent sound speed profile or a range-dependent ground impedance.

Additionally, the Normal Modes method is similar to the FFP method as it implements an integral transform technique too. In contrast to FFP though, this method utilizes a complex contour integration to reduce the integral representation to a sum of residues [12]. Raspet et al. [13] were the first to employ

the normal modes method to predict low-frequency sound propagation in an atmosphere with downward refraction and over a complex impedance ground surface. This choice was made due to the unsatisfactory results obtained from ray tracing approaches under these specific conditions.

Boath FFP and Normal Modes methods can be extended to range dependent environments by dividing the environment into range-independent sectors and then coupling the solutions of those sectors [14]. The generalization of the Normal Modes Method to range dependent environments is known as the Coupled Modes method [15]. The solution within a range-independent segment is constructed using the standard normal-mode solution and interface conditions (continuity of pressure and radial velocity) are then used to "glue" the solutions together. This coupled-mode approach is straightforward but leads to a computationally intensive procedure [16].

The Linearized Euler Equations (LEEs) are a more advanced method for simulating sound propagation, derived by applying basic aeroacoustics assumptions to the Euler Equations. This method is computationally more demanding but offers greater accuracy. The LEEs are typically solved using either the finite volumes or finite differences method [17]. When time-domain solutions are required using the finite differences method, it is referred to as the "Finite Difference Time Domain method" or "FDTD method". However, it is important to note that the LEEs method involves computationally intensive calculations, particularly when modeling finite ground impedance is necessary. These calculations can be time-consuming, adding to the complexity and computational demands of the simulation process.

Historically, the Parabolic Equation method was first introduced in electromagnetic wave propagation applications [18]. In the area of acoustics, it was primarily used in underwater cases [19]. In 1989, Gilbert and White introduced a PE technique for studying atmospheric acoustics [20]. This technique is known as the Crank-Nicholson PE (CNPE) method, which is a finite difference method named by the Crank-Nicholson scheme used for the numerical integration in the parabolic direction. In the present work the CNPE method was implemented based on the description provided by West et al. [21].

The sound field in the PE method is determined by solving a parabolic equation. This equation is derived from the wave equation by excluding the contributions of sound waves with significant elevation angles to the field. It is used to estimate the sound distribution generated by a single source in a refracting atmosphere above the ground surface. This method allows for variations in the sound speed profile and ground impedance along the propagation path. Additionally, the PE method can incorporate the influence of atmospheric turbulence and irregular terrain, two aspects that will be demonstrated in the upcoming chapters.

An alternative approach in solving the parabolic equation is the Green's Function Parabolic Equation (GFPE) method [22]. Although both CNPE and GFPE were developed initially as 2D axisymmetric approaches using the assumption of negligible crosswind and one-way wave propagation, they can also be formulated to 3D [23]. The Green's Function method is faster that the Crank-Nicolson method as it is not based on a finite difference range step limited to a fraction of a wavelength but utilizes range steps many wavelengths long. However, it less accurate than CNPE in cases with wide-angle propagation and large sound speed gradients.

The parabolic approach is valid in flat terrain cases where back scattering does not occur. In cases of irregular terrain, the parabolic approach may be valid provided the local slopes do not exceed 30°. In

such cases an effective approach is the implementation of the Generalized Terrain Parabolic Equation (GTPE) method [24].

According to this approach a transformation of coordinates is applied, following the terrain profile by utilizing a new matrix-vector parabolic equation with elements that depend on range. The primary objective of this study is to create an efficient model capable of simulating the propagation of noise in the atmospheric environment, specifically considering complex terrains along with the influence of atmospheric turbulence. For this reason, the Generalized Terrain Parabolic Equation method was chosen. The reason for selecting this method is its low computational demands due to the parabolic and axisymmetric assumptions. Therefore, it is a good compromise between accuracy and computational cost for smooth terrain variations. In addition, it is a frequency-domain method which allows for choosing a different space discretization according to the frequency of interest.

Compared to the previous diploma thesis of Mrs. Kappatou [25], in which the Parabolic Equation Method was applied in flat terrain, in the present work the effects of irregular terrain and atmospheric turbulence have been incorporated. This dissertation starts with Chapter 2, where the Mathematical formulation of the Generalized Terrain Parabolic Equation is presented, mainly focused on the transformation of the Helmholtz Equation. It also includes the theoretical basis for the integration of atmospheric turbulence to the PE using fields of refractive-index fluctuations. In Chapter 3 the numerical implementation is described, including the discretization of the transformed Parabolic Equation along with the appropriate boundary conditions both on ground and on the upper boundary, combined with any atmospheric losses that will be considered. Chapter 4 describes the application of the GTPE method and the turbulent PE and includes comparisons with results of other methods along with measurements and predictions. Finally, in Chapter 5 the conclusions of this study are summarized together with future work suggestions.

2. Mathematical Formulation

2.1 Generalized Terrain Parabolic Equation

In this section the mathematical basis of the Generalized Terrain Parabolic Equation method according to [16, App. M.3, "Generalized Terrain PE (GTPE) method", pg. 267-277] is described. The GTPE method is a 2D axisymmetric approach. That means that it uses a rectangular xz coordinate system in which both the source and the receiver are included. The x-coordinate denotes the horizontal range, while the z is the vertical coordinate (Fig.1). To describe the terrain profile a function is used

$$z = H(x) \tag{2.1}$$

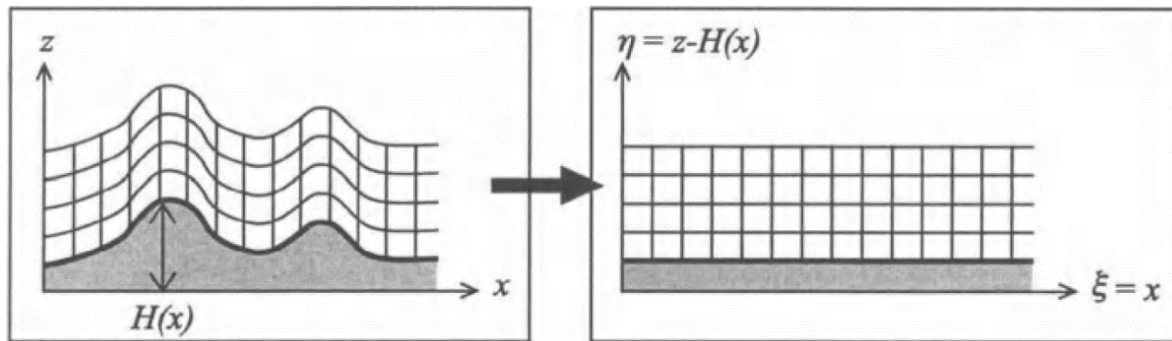where $H(x)$ is the height of the terrain at point x.

Figure 1: Coordinate transformation grids. On the left the original xz physical domain and on the right the $\xi\eta$ computational domain. Source: [16, pg.267]

The core of the GTPE method is the coordinate transformation (2.2), in which each point (x, z) from the initial physical domain is mapped to a point (ξ, η) in the computational domain.

$$\xi = x \tag{2.2}$$
$$\eta = z - H(x)$$

Another essential aspect of GTPE is the treatment of the ground surface boundary condition. This involves the determination of the fluid velocity component perpendicular to the ground surface, which is crucial for establishing a relationship with pressure. For that but also additional reasons, the first $dH/dx = dH/d\xi$ and second $d^2H/dx^2 = d^2H/d\xi^2$ derivatives, denoted as H' and H'' accordingly need to be calculated.

Due to the axisymmetric assumption, the three-dimensional Helmholtz equation reduces to the two-dimensional Helmholtz equation

$$\frac{d^2q}{dx^2} + \frac{d^2q}{dz^2} + k^2q = 0 \tag{2.3}$$

with $q = p\sqrt{x}$, where p is the complex pressure amplitude. In order to perform the transformation $(x, z) \rightarrow (\xi, \eta)$ of the Helmholtz equation the definition of the partial derivative operators of x and z with respect to the operators of the transformed coordinates ξ and η is needed. The notation that will be used is $\partial_x = \partial/\partial x$ and $\partial_x^2 = \partial^2/\partial x^2$ and similarly for the z, ξ and η. Equations (2.3) are derived from Eq.(2.2)

$$
\begin{aligned}
\partial_z &= \partial_\eta \\
\partial_z^2 &= \partial_\eta^2 \\
\partial_x &= \partial_\xi - H'\partial_\eta \\
\partial_x^2 &= \partial_\xi^2 - 2H'\partial_{\xi\eta}^2 - H''\partial_\eta + H'^2\partial_\eta^2.
\end{aligned}
\tag{2.4}
$$

Then, combining (2.3) and (2.4) yields the Helmholtz equation in the $\xi\eta$ computational coordinate system

$$
\partial_\xi^2 q - 2H'\partial_{\xi\eta}^2 q - H''\partial_\eta q + (H'^2 + 1)\partial_\eta^2 q + k^2 q = 0.
\tag{2.5}
$$

For additional numerical accuracy the solution is written as

$$
q(\xi, \eta) = \psi(\xi, \eta)\exp(ik_a\xi)
\tag{2.6}
$$

where k_a is the wave number at the ground surface. Substitution of Eq. (2.6) into (2.5) gives

$$
\begin{aligned}
\partial_\xi^2\psi + 2ik_a\partial_\xi\psi - 2H'\big(\partial_{\xi\eta}^2\psi + ik_a\partial_\eta\psi\big) - H''\partial_\eta\psi + (H'^2 + 1)\partial_\eta^2\psi \\
+ (k^2 - k_a^2)\psi = 0.
\end{aligned}
\tag{2.7}
$$

Despite the fact that the second-order GTPE will be implemented in this work, it is needed first to elaborate on the first-order GTPE. The latter is obtained by neglecting the terms $\partial_\xi^2\psi$ and $\partial_{\xi\eta}^2\psi$ from Eq. (2.7)

$$
\partial_\xi\psi = \frac{i}{2k_a}L_1(\psi)
\tag{2.8}
$$

where the operate L_1 is defined as

$$
L_1 = \alpha\partial_\eta^2 - \beta\partial_\eta + \gamma
\tag{2.9}
$$

and

$$
\begin{aligned}
\alpha(\xi) &= H'^2 + 1 \\
\beta(\xi) &= 2ik_aH' + H'' \\
\gamma(\eta) &= k^2(\eta) - k_a^2
\end{aligned}
\tag{2.10}
$$

For the second-order GTPE Equation (2.7) is integrated over one range step from $\xi = a$ to $\xi = b$, with $b = a + \Delta\xi$. For the integral of the term $\partial_\xi^2\psi$ the first-order solution (2.8) is used while the term $\partial_{\xi\eta}^2$ is integrated by parts. In this way the second-order GTPE is produced

$$\left[\frac{i}{2k_a}L_1(\psi) + 2ik_a\psi - 2H'\partial_\eta\psi\right]_a^b + I_\alpha + I_\chi + I_\gamma = 0 \tag{2.11}$$

with

$$I_\alpha = \int_a^b \alpha(\xi)\,\partial_\eta^2\psi\,d\xi$$
$$I_\chi = \int_a^b \chi(\xi)\,\partial_\eta\psi\,d\xi \tag{2.12}$$
$$I_\gamma = \int_a^b \gamma(\eta)\,\psi\,d\xi$$

where α and γ are given by Eq.(2.10), while χ is given by

$$\chi(\xi) = H'' - 2ik_aH' \tag{2.13}$$

2.2 Atmospheric turbulence in the PE method

2.2.1 Turbulence in sound propagation models

The GTPE method utilizes vertical temperature and wind velocity profiles to represent the atmosphere. The assumption made was that these profiles remained constant over time. However, in reality, these profiles undergo continuous changes. These changes can occur gradually over hours or even longer periods, known as slow variations. Additionally, there are faster variations or fluctuations that happen on shorter time scales, such as seconds or minutes. These rapid fluctuations are commonly known as atmospheric turbulence [26]. The description of atmospheric turbulence will follow the structure of [16, App. I & App. J, pg. 203-229].

In models of atmospheric sound propagation, the turbulent atmosphere is usually described as a medium with a randomly fluctuating effective sound speed. The effective sound speed is defined as $c_{eff} = c + u$, where c is the adiabatic sound speed and u is the horizontal wind velocity component in the direction of sound propagation. The adiabatic sound speed is related to the temperature T by the relation $c = c_o\sqrt{T/T_o}$, where c_o is the sound speed at a reference temperature T_o. Values of $c_o = 331\,m/s$ and $T_o = 273K$ are usually used. Turbulent fluctuations of the temperature T and the wind velocity component u correspond to turbulent fluctuations of the effective sound speed c_{eff}. A quantity that is equivalent to the effective sound speed is the (acoustic) refractive index $n = c_o/c_{eff}$. In a turbulent atmosphere, the refractive index fluctuates at each point around an average value, which is of the order of unity. The average value is denoted as $\bar{n}$ and the fluctuation is denoted as μ. Thus,

$$n = \bar{n} + \mu \tag{2.14}$$

with $\mu \ll \bar{n}$ and $\bar{\mu} = 0$. The fluctuation μ is related to the turbulent temperature fluctuation T_t and the turbulent wind velocity u_t by the expression

$$\mu = -\frac{T_t}{2T_o} - \frac{u_t}{c_o} \tag{2.15}$$

which follows from $n = c_o/c_{eff}$ and $c_{eff} = c_o\sqrt{T/T_o} + u$.

In order to simulate atmospheric turbulence, it is assumed that an average sound pressure field over a short period of time can be approximated by a (logarithmic) average of a set of sound pressure fields, computed for a set of random realizations of the turbulent atmosphere.

The random realizations of the turbulent atmosphere are represented by random fields of the refractive-index fluctuations μ. The sound pressure fields for different random fields can be computed with the PE method while the random fields are calculated with the aid of a random number generator. The calculation takes into account the condition that the correlation function of the refractive-index fluctuations should have the correct value.

2.2.2 Random fields

The wind velocity components and the temperature in the turbulent atmosphere are rapidly fluctuating functions of position and time. These functions are called random functions. The fields of the wind velocity components and the temperature are called random fields. Random fields can be characterized by a correlation function or a structure function along with the related spectral densities [27].

The time average of a random function $f(\boldsymbol{r})$ is denoted as $\overline{f(\boldsymbol{r})}$. In this work only random functions with $\overline{f(\boldsymbol{r})} = 0$ will be considered. An example of a random function with $\overline{f(\boldsymbol{r})} = 0$ is the deviation of the temperature.

The correlation function of a random function $f(\boldsymbol{r})$ is defined as

$$B(\boldsymbol{r}_1, \boldsymbol{r}_2) = \overline{f(\boldsymbol{r}_1)f(\boldsymbol{r}_2)} \tag{2.16}$$

A random function $f(\boldsymbol{r})$ is called homogeneous if the correlation function B depends on $\boldsymbol{r}_1$ and $\boldsymbol{r}_2$ only through the difference $\boldsymbol{r} = \boldsymbol{r}_1 - \boldsymbol{r}_2$, so that $B(\boldsymbol{r}_1, \boldsymbol{r}_2) = B(\boldsymbol{r})$. A homogeneous function $f(\boldsymbol{r})$ is called isotropic if B depends only on the length r of the vector $\boldsymbol{r}$, so that $B(\boldsymbol{r}) = B(r)$.

If the correlation function depends not only on the vector $\boldsymbol{r} = \boldsymbol{r}_1 - \boldsymbol{r}_2$ but also on the position in the atmosphere, the random function is not homogeneous. In this case one can use the structure function, which is defined as

$$D(\boldsymbol{r}_1, \boldsymbol{r}_2) = \overline{[f(\boldsymbol{r}_1) - f(\boldsymbol{r}_2)]^2}. \tag{2.17}$$

Since the structure function contains the difference between the values of the random function at two points, gradual changes in the random field have a smaller effect on the structure function than on the

correlation function. A random function $f(r)$ is called locally homogeneous if $D(r_1, r_2) = D(r)$, with $r = r_1 - r_2$. Additionally, if $D(r) = D(r)$ the random function is called locally isotropic.

The correlation function $B(r)$ and the structure function $D(r)$ of an isotropic random function $f(r)$ are related to each other:

$$D(r) = 2B(0) - 2B(r) \tag{2.18}$$

As follows from Eqs. (2.16) and (2.17). In practice the equality $B(\infty) = 0$ is always true and therefore $D(\infty) = 2B(0)$. This gives

$$B(r) = \frac{1}{2}D(\infty) - \frac{1}{2}D(0) \tag{2.19}$$

The foregoing applies to scalar functions, such as the temperature fluctuation in the atmosphere. The wind velocity fluctuation in the atmosphere however is a vector function. A homogeneous vector function $v(r)$ can be characterized by a set of nine correlation functions

$$B_{ij}(r) = \overline{u_i(r_1)u_j(r_2)} \tag{2.20}$$

and a set of nine structure functions

$$D_{ij}(r) = \overline{[u_i(r_1) - u_i(r_2)][u_j(r_1) - u_j(r_2)]} \tag{2.21}$$

with $r = r_1 - r_2$ and $i, j = 1,2,3$, where u_1, u_2 and u_3 are the x, y and z components of the vector v, respectively. If the vector field is isotropic, the nine correlation functions B_{ij} can all be expressed in two functions, the longitudinal structure function $B_{rr}(r)$ and the transverse correlation function $B_{tt}(r)$:

$$B_{ij}(r) = \left(\delta_{ij} - \frac{r_i r_j}{r^2}\right)B_{tt}(r) + \frac{r_i r_j}{r^2}B_{rr}(r) \tag{2.22}$$

with $r = (r_1, r_2, r_3)$ and $\delta_{ij} = 1$ for $i = j$ and $\delta_{ij} = 0$ for $i \neq j$ [28]. Analogously, the nine structure functions D_{ij} for locally isotropic turbulence ca all be expressed in the longitudinal structure function $D_{rr}(r)$ and the transverse structure function $D_{tt}(r)$:

$$D_{ij}(r) = \left(\delta_{ij} - \frac{r_i r_j}{r^2}\right)D_{tt}(r) + \frac{r_i r_j}{r^2}D_{rr}(r) \tag{2.23}$$

Examples of the longitudinal structure function are $D_{11}(e_x)$, $D_{22}(e_y)$ and $D_{33}(e_z)$ where e_x, e_y and e_z are unit vectors in the x, y and z directions, respectively. Equation (2.23) gives $D_{11}(e_x) = D_{22}(e_y) = D_{33}(e_z)$. An example of the transverse structure function is $D_{11}(e_y)$.

If one assumes that the flow is incompressible ($\nabla \cdot v = 0$), one can derive a relation between $B_{rr}(r)$ and $B_{tt}(r)$, and a relation between $D_{rr}(r)$ and $D_{tt}(r)$:

$$B_{tt}(r) = \frac{1}{2r}\frac{d}{dr}[r^2 B_{rr}(r)] \qquad (2.24)$$

$$D_{tt}(r) = \frac{1}{2r}\frac{d}{dr}[r^2 D_{rr}(r)] \qquad (2.25)$$

In this case, the nine correlation functions can all be expressed in a single function, either $B_{tt}(r)$ or $B_{rr}(r)$, and the nine structure functions can all be expressed in a single function, either $D_{tt}(r)$ or $D_{rr}(r)$

2.2.3 Spectral density

The spectral density of a homogeneous random function $f(\mathbf{r})$ is the special Fourier transform of the correlation function $B(\mathbf{r})$ [27, 28]. One distinguishes one-, two- and three-dimensional spectral densities, to describe correlation along a line, in a plane and in a volume respectively.

In the one-dimensional case, the Fourier transform pair is

$$B(r) = \int_{-\infty}^{\infty} \exp(ikr)\, V(k)dk \qquad (2.26)$$

$$V(k) = \frac{1}{2\pi}\int_{-\infty}^{\infty} \exp(-ikr)\, B(r)dr \qquad (2.27)$$

where $V(k)$ is the one-dimensional spectral density of the random function. In three-dimensional case, the Fourier transform pair is

$$B(\mathbf{r}) = \iiint_{-\infty}^{\infty} \exp(i\mathbf{k}\cdot\mathbf{r})\, \Phi(\mathbf{k})\, d\mathbf{k} \qquad (2.28)$$

$$\Phi(\mathbf{k}) = \frac{1}{(2\pi)^3}\iiint_{-\infty}^{\infty} \exp(-i\mathbf{k}\cdot\mathbf{r})\, B(\mathbf{r})\, d\mathbf{r} \qquad (2.29)$$

where $\Phi(\mathbf{k})$ is the three-dimensional spectral density of the random function and $\mathbf{r}$ and $\mathbf{k}$ are the three-dimensional vectors. If the field is isotropic $B(\mathbf{r}) = B(r)$ and Eq. (2.29) reduces to

$$\Phi(\mathbf{k}) = \frac{1}{2\pi^2 k}\int_{0}^{\infty} \sin(kr)\, B(r)rdr \qquad (2.30)$$

so $\Phi(\mathbf{k}) = \Phi(k)$ al well. Comparison of Eqs. (2.27) and (2.30) yields the relation

$$\Phi(k) = -\frac{1}{2\pi k}\frac{dV(k)}{dk} \qquad (2.31)$$

With this relation one can derive the three-dimensional spectral density of an isotropic random function from the one-dimensional spectral density.

In the two-dimensional case, the Fourier transform pair is

$$B(\boldsymbol{r}) = \iint_{-\infty}^{\infty} \exp(i\boldsymbol{k} \cdot \boldsymbol{r}) \, F(\boldsymbol{k}) d\boldsymbol{k} \tag{2.32}$$

$$F(\boldsymbol{k}) = \frac{1}{(2\pi)^2} \iint_{-\infty}^{\infty} \exp(-i\boldsymbol{k} \cdot \boldsymbol{r}) \, B(\boldsymbol{r}) d\boldsymbol{r} \tag{2.33}$$

where $F(\boldsymbol{k})$ is the two-dimensional spectral density of the random function and $\boldsymbol{r}$ and $\boldsymbol{k}$ are two-dimensional vectors, e.g. $\boldsymbol{r} = (x, z)$ and $\boldsymbol{k} = (k_x, k_z)$. Comparison of Eqs. (2.28) and (2.32) for $\boldsymbol{r} = 0$ yields the relation

$$F(k_x, k_z) = \int_{-\infty}^{\infty} \Phi(k_x, k_y, k_z) \, dk_y \tag{2.34}$$

and analogous relations for $F(k_x, k_y)$ and $F(k_y, k_z)$. If the field is isotropic, Eq. (2.33) reduces to

$$F(\boldsymbol{k}) = \frac{1}{2\pi} \int_0^{\infty} J_o(kr) B(r) r dr \tag{2.35}$$

so $F(\boldsymbol{k}) = F(k)$. J_o is the Bessel function of the first kind.

For vectors functions a set of nine correlation functions $B_{ij}(\boldsymbol{r})$ were defined in Eq. (2.20). Each correlation function $B_{ij}(\boldsymbol{r})$ corresponds to a three-dimensional spectral density $\Phi_{ij}(\boldsymbol{r})$ defined by Eq. (2.29) (with $\Phi_{ij} = \Phi$ and $B_{ij} = B$) and a two-dimensional spectral density $F_{ij}(\boldsymbol{k})$ defined by Eq. (2.33) (with $F_{ij} = F$ and $B_{ij} = B$).

2.2.4 Gaussian, Kolmogorov and von Karman spectra

In the acoustic literature [29], various mathematical functions have been used to approximate the statistical functions $B(\boldsymbol{r}), D(\boldsymbol{r}), V(k), F(\boldsymbol{r})$ and $\Phi(\boldsymbol{r})$ of the refractive-index fluctuation μ. A Gaussian function has been widely used. A Gaussian correlation function corresponds to Gaussian spectral densities. In this case the atmosphere is referred to as an atmosphere with a Gaussian spectrum of refractive-index fluctuations. A more realistic representation is the von Karman spectrum, which is related to the Kolmogorov spectrum.

First, cases with atmosphere with only temperature fluctuations ($u_t = 0$) will be considered. From Eq. (2.15) the relation $\mu = -\frac{1}{2}T_t/T_o$ can be derived. This implies $B(\boldsymbol{r}) = \frac{1}{4}B_T(\boldsymbol{r})/T_o^2$, where $B_T(\boldsymbol{r})$ is the correlation function of the temperature fluctuations. For isotropic turbulence $B_T(\boldsymbol{r}) = B_T(r)$, which implies $B(\boldsymbol{r}) = B(r)$. In the same way $D(\boldsymbol{r}) = D(r)$, $F(\boldsymbol{r}) = F(r)$ and $\Phi(\boldsymbol{r}) = \Phi(r)$.

For the calculation of the refractive-index fluctuation field μ only the two-dimensional spectral density F will be used, so only these functions will be presented for each type of spectrum.

For the Gaussian spectrum, the two-dimensional spectral density is given by the following expression:

$$F(k) = \mu_o^2 \frac{a^2}{4\pi} \exp\left(-k^2\, a^2/4\right) \tag{2.36}$$

where a is the correlation length and μ_o is the standard deviation of μ. The standard deviation μ_o is related to the standard deviation σ_T of the temperature fluctuations by the expression $\mu_o = \frac{1}{2}\sigma_T/T_o$, which follows from the expression $\mu = -\frac{1}{2}T_t/T_o$. The proof of this expression can be found in [16, App. I, pg. 212-213].

The Gaussian spectrum has been widely used in atmospheric acoustics, with a value of about $1m$ for the correlation length a and values ranging from about 10^{-6} to 10^{-5} for the variance μ_o^2 [30].

For the Kolmogorov spectrum the expression is

$$F(k) = C^2 \frac{\Gamma^2\left(\frac{1}{2}p + 1\right) 2^p}{2\pi^2} \sin\left(\frac{1}{2}\pi\, p\right) |k|^{-p-2} \tag{2.37}$$

with $p = 2/3$; here Γ is the gamma function. C^2 is defined as $C^2 = C^3(15v)^2 l_o^{-8/3}$, where C is a dimensionless constant of the order of unity [27], v is the kinematic viscosity and l_o is called the inner scale of turbulence and is typically of the order of $1mm$.

For the von Karman spectrum the expression is

$$F(k) = \mu_o^2 \frac{\Gamma(8/6)}{\Gamma(1/3)\pi} \frac{a^2}{(1 + k^2 a^2)^{8/6}} \tag{2.38}$$

where a is the correlation length and μ_o the standard deviation of μ. For $r \ll a$ the von Karman spectrum is of the same form as the Kolmogorov spectrum.

Expressions for the statistical functions of refractive-index fluctuations in an isotropic turbulent atmosphere with wind and temperature fluctuations ($u_t \neq 0$) have different relations. These expressions were developed by Ostashev [29].

From Eq. (2.15) the relation $\mu = -\frac{1}{2}T_t/T_o - u_t/c_o$ can be derived. Consequently, the correlation function $B(r)$ of the refractive-index fluctuation μ is related to the correlation function $B_T(r)$ of the temperature fluctuation T_t and the correlation function $B_{11}(r)$ of the wind velocity fluctuation u_t (Eq. 2.20), by the equation

$$B(\mathbf{r}) = \frac{B_T(\mathbf{r})}{4T_o^2} + \frac{B_{11}(\mathbf{r})}{c_o^2} \tag{2.39}$$

The analogous equation for the spectral density is $F(\mathbf{k}) = F_T(\mathbf{k})/(4T_o^2) + F_{11}(\mathbf{k})/c_o^2$. The indices 11 of F_{11} corresponds to the x coordinate of a rectangular xyz coordinate system, where the x direction is the direction of sound propagation. The functions $B(\mathbf{r})$ and $F(\mathbf{k})$ are anisotropic in this case, due to the anisotropy of the functions $B_{11}(\mathbf{r})$ and $F_{11}(\mathbf{k})$. Although the wind and temperature fluctuations are still assumed to be isotropic, the effective sound speed for propagation in the x direction and the corresponding refractive-index fluctuations are anisotropic. Below the fluctuations $F(k_x, k_z) = F(k_x, k_y)$ and $F(k_y, k_z)$ for the Gaussian spectrum and the von Karman spectrum are presented. Because of the anisotropy we indicate the components of the vectors $\mathbf{r}$ and $\mathbf{k}$ explicitly in the arguments of the functions. The function $F(k_x, k_z)$ will be used later for the calculation of sound propagation in a turbulent atmosphere.

For the Gaussian spectrum, with a Gaussian temperature correlation function $B_T(r) = \sigma_T^2 \exp(-r^2/a^2)$ and a Gaussian longitudinal wind velocity correlation function $B_{rr}(r) = \sigma_v^2 \exp(-r^2/a^2)$, the two-dimensional spectral densities $F(k_x, k_z)$ and $F(k_y, k_z)$, for the Gaussian spectrum are given by

$$F(k_x, k_z) = \frac{a^2}{4\pi}\left(\frac{\sigma_T^2}{4T_o^2} + \frac{\sigma_v^2[\sigma_v^2 a^2 + 2]}{4c_o^2}\right)\exp(-k^2 a^2/4) \tag{2.40}$$

with $k^2 = k_x^2 + k_z^2$, and

$$F(k_y, k_z) = \frac{a^2}{4\pi}\left(\frac{\sigma_T^2}{4T_o^2} + \frac{\sigma_v^2[\sigma_v^2 a^2 + 2]}{4c_o^2}\right)\exp(-k^2 a^2/4) \tag{2.41}$$

with $k^2 = k_y^2 + k_z^2$, where a is the correlation length and σ_T and σ_v are the standard deviation of the temperature and wind velocity fluctuations, respectively.

For the von Karman spectrum, the two-dimensional spectral densities $F(k_x, k_z)$ and $F(k_y, k_z)$ are given by

$$F(k_x, k_z) = \frac{A}{(k^2 + K_o^2)^{8/6}}\left(\frac{\Gamma\left(\frac{1}{2}\right)\Gamma\left(\frac{8}{6}\right)}{\Gamma\left(\frac{11}{6}\right)}\frac{C_T^2}{4T_o^2}\right.$$
$$\left. + \left[\frac{\Gamma\left(\frac{3}{2}\right)\Gamma\left(\frac{8}{6}\right)}{\Gamma\left(\frac{17}{6}\right)} + \frac{k_z^2}{k^2 + K_o^2}\frac{\Gamma\left(\frac{1}{2}\right)\Gamma\left(\frac{14}{6}\right)}{\Gamma\left(\frac{17}{6}\right)}\right]\frac{22C_v^2}{12c_o^2}\right) \tag{2.42}$$

with $k^2 = k_x^2 + k_z^2$, and

$$F(k_y, k_z) = \frac{A}{(k^2 + K_o^2)^{8/6}} \left(\frac{\Gamma\left(\frac{1}{2}\right)\Gamma\left(\frac{8}{6}\right)}{\Gamma\left(\frac{11}{6}\right)} \frac{C_T^2}{4T_o^2} \right.$$
$$\left. + \left[\frac{\Gamma\left(\frac{3}{2}\right)\Gamma\left(\frac{8}{6}\right)}{\Gamma\left(\frac{17}{6}\right)} + \frac{k^2}{k^2 + K_o^2} \frac{\Gamma\left(\frac{1}{2}\right)\Gamma\left(\frac{14}{6}\right)}{\Gamma\left(\frac{17}{6}\right)} \right] \frac{22C_v^2}{12c_o^2} \right) \tag{2.43}$$

with $k^2 = k_y^2 + k_z^2$. $K_o = 2\pi/L$ is related to the size L of the largest eddies, C_T^2 and C_v^2 are the structure parameters of the temperature and wind velocity fluctuations respectively. Here the constant $A = 5/[18\pi\Gamma(1/3)] \approx 0.0330$ is introduced.

2.2.5 Turbulent phase factor in the PE method

In this section the incorporation of atmospheric turbulence in the Crank-Nicolson Parabolic Equation (CNPE) method [31] is described. CNPE is a specific variation of GTPE method where only flat terrain cases can be considered. The basic concept for turbulence in GTPE is similar. In the two-dimensional PE methods, the sound field is represented by the complex pressure amplitude $p(r,z)$ in the rz plane through the source and the receiver. The computation of the field is based on the following one-way wave equation for the quantity $q(r,z) = p(r,z)\sqrt{r}$:

$$\partial_r q(r,z) - iH_1(z)q(r,z) = 0 \tag{2.44}$$

where

$$H_1(z) = \sqrt{k^2(z) + \partial_z^2} \tag{2.45}$$

is the square root operator. The formal solution of Eq. (2.44) is

$$q(r + \Delta r, z) = exp(iH_1\Delta r)q(r,z) \tag{2.46}$$

The corresponding expression for the quantity $\psi(r,z) = q(r,z)exp(-ik_a r)$ is

$$\psi(r + \Delta r, z) = exp(iH_1\Delta r - ik_a\Delta r)\psi(r,z) \tag{2.47}$$

where k_a is the wave number on the ground.

The acoustic refractive index n can be written as $n = \bar{n} + \mu$ with $\mu \ll \bar{n}$ and $\bar{\mu} = 0$. From the relation $n \approx k/k_a$:

$$k = \bar{k} + k_a\mu \tag{2.48}$$

with $\bar{k} = k_a\bar{n}$. In the PE method it is assumed that $\bar{n}$ and $\bar{k}$ are functions of the height z only (within a range step). Substitution of Eq. (2.48) into Eq. (2.45) gives

$$H_1 \approx \sqrt{\bar{k}^2 + 2\bar{k}k_a\mu + \partial_z^2} \tag{2.49}$$

where a term of the order of μ^2 is neglected. A first order expansion of the square root function gives

$$H_1 \approx \overline{H_1} + k_a\mu \tag{2.50}$$

with

$$\overline{H_1} \approx \sqrt{\bar{k}^2 + \partial_z^2} \tag{2.51}$$

In Eq. (2.50) the approximation $\overline{H_1} \approx k_a$ is used. Substitution of Eq. (2.50) into Eq. (2.47) gives

$$\psi(r + \Delta r, z) = exp(i\overline{H_1}\Delta r - ik_a\Delta r)exp(ik_a\mu\Delta r)\psi(r,z) \tag{2.52}$$

The first exponential factor on the right-hand side represents the solution for a non-turbulent atmosphere. The second exponential factor represents the effect of atmospheric turbulence. As μ is real, the second factor is a phase factor.

Hence, turbulence is considered by multiplication of the field by a z-dependent phase factor after each PE range step. This is computationally more efficient than changing the sound speed profile after each PE step.

A slightly more accurate approach is to split the turbulent phase factor into two factors [57]:

$$\psi(r + \Delta r, z) = exp\left(\frac{1}{2}ik_a\mu\Delta r\right)exp(i\overline{H_1}\Delta r$$
$$- ik_a\Delta r)exp\left(\frac{1}{2}ik_a\mu\Delta r\right)\psi(r,z) \tag{2.53}$$

Thus, half of the turbulent phase shift is applied before the 'non-turbulent PE step' and the other half is applied after the step. In a sequence of PE steps, a step from range r to range $r + \Delta r$ ends with multiplication by the turbulent phase factor $exp\left(\frac{1}{2}ik_a\mu(r,z)\Delta r\right)$, and the next step from range $r + \Delta r$ to range $r + 2\Delta r$ begins with multiplication by the factor $exp\left(\frac{1}{2}ik_a\mu(r + \Delta r, z)\Delta r\right)$. This is equivalent to multiplication by a single factor

$$exp(ik_a\mu_2\Delta r) \tag{2.54}$$

between the two successive PE steps, where μ_2 is given by

$$\mu_2 = \frac{1}{2}[\mu(r,z) + \mu(r + \Delta r, z)] \tag{2.55}$$

In the CNPE method, the range step Δr is usually small compared with the turbulent correlation length, so turbulent fluctuations are accurately sampled. In the GTPE method the same methodology is applied, with the additional exponential terms being multiplied by the new solution for each range step.

The expressions derived above for the turbulent phase factor contain the field of refractive-index fluctuations $\mu(r, z)$ in the rz plane. Realizations of the random field $\mu(r, z)$ can be calculated with a random number generator, in such a way that the field has the correct value of the correlation function $B(\boldsymbol{s}) = \overline{\mu(\boldsymbol{r} + \boldsymbol{s})\mu(\boldsymbol{r})}$ [25, 72]. It is assumed that the random field $\mu(r, z)$ is homogeneous.

From Eq. (2.32):

$$B(\boldsymbol{s}) = \iint_{-\infty}^{\infty} \cos(\boldsymbol{k} \cdot \boldsymbol{s}) F(\boldsymbol{k}) d\boldsymbol{k} \tag{2.56}$$

where $F(\boldsymbol{k})$ is the two-dimensional spectral density of the refractive-index fluctuations in the rz plane; from previous section $F(\boldsymbol{k}) = F(k_x, k_z)$ (the horizontal r coordinate used here corresponds to the horizontal x coordinate). The exponential function in Eq. (2.32) has been replaced by a cosine function, as $F(\boldsymbol{k})$ is an even function of the components of vector $\boldsymbol{k}$. Polar $k\theta$ coordinates are introduced for the vector $\boldsymbol{k}$, so Eq. (2.56) can be written as

$$B(\boldsymbol{s}) = \int_0^{2\pi} \int_0^{\infty} \cos(\boldsymbol{k} \cdot \boldsymbol{s}) F(\boldsymbol{k}) k \, dk \, d\theta \tag{2.57}$$

with $\boldsymbol{k} = (k \, cos\theta, k \, sin\theta)$. The integration over the angle θ can be replaced by 2π times the average over θ:

$$B(\boldsymbol{s}) = 2\pi < \int_0^{\infty} \cos(\boldsymbol{k} \cdot \boldsymbol{s}) F(\boldsymbol{k}) k \, dk >_\theta \tag{2.58}$$

where the brackets $< . >_\theta$ denote the average over the angle θ. The integral is approximated by a finite sum:

$$B(\boldsymbol{s}) = 2\pi < \Delta k \sum_n \cos(\boldsymbol{k}_n \cdot \boldsymbol{s}) F(\boldsymbol{k}_n) k_n >_\theta \tag{2.59}$$

with discrete wave number vectors $\boldsymbol{k}_n$. If the definition of the correlation function is used,

$$B(\boldsymbol{s}) = < \mu(\boldsymbol{r} + \boldsymbol{s})\mu(\boldsymbol{r}) >_\theta \tag{2.60}$$

then it is demonstrated that the random field of μ given by Eq. (2.61), corresponds to the correlation function of Eq. (2.59). The proof for derivation of Eq. (2.61) can be found in [16, App I, pg. 225]. The random realizations of the corresponding random field $\mu(\boldsymbol{r})$ is given by:

$$\mu(\boldsymbol{r}) = \sqrt{4\pi\Delta k} \sum_n \cos(\boldsymbol{k}_n \cdot \boldsymbol{r} + a_n)\sqrt{F(\boldsymbol{k}_n)k_n} \tag{2.61}$$

with $\boldsymbol{k}_n = (k_n \, cos\theta_n, k_n \, sin\theta_n)$ and $k_n = n\Delta k$ for $n = 1, 2, \dots, N$; here θ_n and α_n are random angles between 0 and 2π. Thus, the field $\mu(\boldsymbol{r})$ is calculated by superposition of N harmonic functions, or 'modes', with regularly spaced wave numbers k_n, random polar angles θ_n and random phase angles a_n.

In the CNPE method a rectangular grid in the rz plane is used, through the source and the receiver. Turbulence is incorporated by multiplication of the field $\psi(r, z_j)$ at the grid points (r, z_j) by the phase factor given by Eq. (2.53), after each range step. This requires the evaluation of the refractive-index fluctuations $\mu(r, z_j)$ at the grid points. From Eq. (2.61):

$$\mu(r, z_j) = \sum_n G(\mathbf{k}_n) \cos(rk_{nr} + z_j k_{nz} + a_n) \tag{2.62}$$

with $G(\mathbf{k}_n) = \sqrt{4\pi \, \Delta k \, F(\mathbf{k}_n) k_n}$, $k_{nr} = k_n \cos\theta_n$ and $k_{nz} = k_n \sin\theta_n$. As the calculation of the cosine function for all grid points in time-consuming, the cosine term can be rewritten as

$$\cos(rk_{nr} + z_j k_{nz} + a_n) = Re\{exp(ik_{nr}r + ia_n)[exp(ik_{nz}\Delta z)]^j\} \tag{2.63}$$

where $z_j = j\Delta z$. The two exponential factors on the right-hand side are independent of z_j, so the cosine factors for fixed r and n can be calculated efficiently for all z_j by repeated multiplication by the constant factor $exp(ik_{nz}\Delta z)$.

3. Numerical Simulation

3.1 PE Discretization

In this section the numerical implementation of GTPE method is described according to [16, App. M.3, "Generalized Terrain PE (GTPE) method", pg. 267-277]. The three integrals in Eqs. (2.12) can be written as

$$I_R = \int_a^b R(\xi)\, \partial_\eta^n \psi\, d\xi \tag{3.1}$$

with $n = 2$ for $R = \alpha$, $n = 1$ for $R = \chi$ and $n = 0$ for $R = \gamma$. The three integrals I_R are approximated by assuming a linear variation of $\partial_\eta^n \psi$ with ξ over the range from $\xi = a$ to $\xi = b$:

$$\partial_\eta^n \psi(\xi) = \frac{b-\xi}{\Delta\xi}\, \partial_\eta^n \psi(a) + \frac{\xi-a}{\Delta\xi}\, \partial_\eta^n \psi(b) \tag{3.2}$$

Substitution of Eq. (3.2) into Eq. (3.1) gives

$$I_R = A_R\, \partial_\eta^n \psi(a) + B_R\, \partial_\eta^n \psi(b) \tag{3.3}$$

with

$$A_R = \frac{1}{\Delta\xi} \int_a^b (b-\xi)\, R(\xi)\, d\xi$$
$$B_R = \frac{1}{\Delta\xi} \int_a^b (\xi-a)\, R(\xi)\, d\xi \tag{3.4}$$

These integrals are approximated by assuming a linear variation of R with ξ over the range step from $\xi = a$ to $\xi = b$:

$$R(\xi) = \frac{b-\xi}{\Delta\xi} R(a) + \frac{\xi-a}{\Delta\xi} R(b) \tag{3.5}$$

This gives

$$A_R = \Delta\xi \left[\frac{1}{3} R(a) + \frac{1}{6} R(b) \right]$$
$$B_R = \Delta\xi \left[\frac{1}{6} R(a) + \frac{1}{3} R(b) \right] \tag{3.6}$$

The second-order GTPE (Eq. 2.11) can be solved numerically by approximating the vertical derivatives $\partial_\eta^2 \psi$ and $\partial_\eta \psi$ with finite differences. The grid shown in Fig. 1 is used, with grid points at heights

$$\eta_j = j\,\Delta\eta \;\; with\; j = 1, 2, \dots, M \tag{3.7}$$

where $\Delta\eta$ is the vertical grid spacing. The field ψ at range ξ is denoted as a vector $\vec{\psi}(\xi)$ with elements $\psi_j = \psi(\xi, \eta_j)$. Using the central difference formulas

$$(\partial_\eta \psi)_{\eta_j} = \frac{\psi_{j+1} - \psi_{j-1}}{2\Delta\eta}$$
$$(\partial_\eta^2 \psi)_{\eta_j} = \frac{\psi_{j+1} - 2\psi_j + \psi_{j-1}}{(\Delta\eta)^2} \tag{3.8}$$

the Eq. (2.11) is written as

$$\boldsymbol{M_2}\vec{\psi}(b) = \boldsymbol{M_1}\vec{\psi}(a) \tag{3.9}$$

where $\boldsymbol{M_1}$ and $\boldsymbol{M_2}$ are triagonal matrices given by

$$\boldsymbol{M_1} = c_3\,\boldsymbol{\delta}^2 + c_2\boldsymbol{\delta} + \boldsymbol{c_1}$$
$$\boldsymbol{M_2} = d_3\,\boldsymbol{\delta}^2 + d_2\boldsymbol{\delta} + \boldsymbol{d_1} \tag{3.10}$$

The quantities $\boldsymbol{c_1}$, c_2 and c_3 are given by

$$c_3 = \frac{1}{2ik_\alpha\,(\Delta\eta)^2}\left(\frac{i\alpha}{2k_\alpha} + B_\alpha\right)$$
$$c_2 = -\frac{1}{2ik_\alpha\,\Delta\eta}\left(\frac{i\beta}{2k_\alpha} + 2H' - B_\chi\right) \tag{3.11}$$
$$\boldsymbol{c_1} = 1 + \frac{\boldsymbol{\gamma}}{4k_\alpha^2} + \frac{B_\gamma}{2ik_\alpha}$$

where α, β and H' are evaluated at $\xi = b$. The quantities $\boldsymbol{d_1}$, d_2 and d_3 are given by

$$d_3 = \frac{1}{2ik_\alpha\,(\Delta\eta)^2}\left(\frac{i\alpha}{2k_\alpha} - A_\alpha\right)$$
$$d_2 = -\frac{1}{2ik_\alpha\,\Delta\eta}\left(\frac{i\beta}{2k_\alpha} + 2H' + A_\chi\right) \tag{3.12}$$
$$\boldsymbol{d_1} = 1 + \frac{\boldsymbol{\gamma}}{4k_\alpha^2} - \frac{A_\gamma}{2ik_\alpha}$$

where α, β and H' are evaluated at $\xi = a$. The quantities $\boldsymbol{\gamma}$, $\boldsymbol{A_\gamma}$, $\boldsymbol{B_\gamma}$, $\boldsymbol{c_1}$ and $\boldsymbol{d_1}$ are diagonal matrices. The quantities $\boldsymbol{\delta}^2$ and $\boldsymbol{\delta}$ are triagonal matrices given by

$$\boldsymbol{\delta}^2 = \begin{pmatrix} -2 & 1 & & & & \\ 1 & -2 & 1 & & & \\ & 1 & -2 & 1 & & \\ & & \ddots & \ddots & \ddots & \\ & & & 1 & -2 & 1 \\ & & & & 1 & -2 \end{pmatrix} \tag{3.13}$$

$$\delta = \begin{pmatrix} 0 & 1 & & & & \\ -1 & 0 & 1 & & & \\ & -1 & 0 & 1 & & \\ & & \ddots & \ddots & \ddots & \\ & & & -1 & 0 & 1 \\ & & & & -1 & 0 \end{pmatrix} \qquad (3.14)$$

Here the boundary conditions at the ground surface and at the top of the grid were ignored. These conditions will be considered in the following section.

3.2 Boundary conditions

At the ground surface the local reaction boundary condition is used

$$\left(\frac{p}{u_n}\right)_{\eta=0} = Z \, \rho c \qquad (3.15)$$

where Z is the normalizes ground impedance, ρc is the impedance of air (evaluated just above the ground surface), p is the complex pressure amplitude $(p \equiv p_c)$ and u_n is the component of the complex velocity amplitude normal to the ground surface, in downward direction $(u_n \equiv u_{c,n})$.

Writing the pressure and velocity fields respectively as:

$$p = Re\{p_c \, e^{-i\omega t}\} \qquad (3.16)$$

$$\vec{v} = Re\{\vec{v}_c \, e^{-i\omega t}\} \qquad (3.17)$$

the linear acoustic equation for momentum conservation can be expresses in the following simplified form

$$u_n = \frac{1}{i\omega\rho} \frac{\partial p}{\partial \boldsymbol{n}} \qquad (3.18)$$

with

$$\frac{\partial p}{\partial \boldsymbol{n}} = n_x \frac{\partial p}{\partial x} + n_z \frac{\partial p}{\partial z} \qquad (3.19)$$

where $\boldsymbol{n} = (n_x, n_z)$ is the unit normal vector at the ground surface, in downward direction (Fig. 2). So

$$\boldsymbol{n} = (sin \, a_H, -cos \, a_H) \qquad (3.20)$$

where a_H is the local elevation angle of the ground surface, which satisfies

$$tan \, a_H = H'(x) \qquad (3.21)$$

Using Eqs. (2.4), Equation (3.17) give

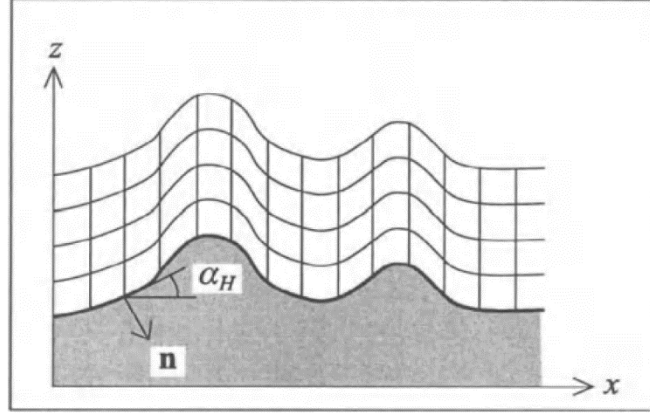$$\frac{\partial p}{\partial \boldsymbol{n}} = n_x \frac{\partial p}{\partial x} + n_z \frac{\partial p}{\partial z}$$

(3.22)

Figure 2: Unit normal vector **n** and local elevation angle a_H of the ground surface, used for the boundary condition at the ground surface. Source: [16, pg.273]

The boundary condition (3.15) becomes

$$\frac{ik_0}{Z} p_0 = \sin a_H \left(\frac{\partial p}{\partial \xi}\right)_{\eta=0} - \frac{1}{\cos a_H} \left(\frac{\partial p}{\partial \eta}\right)_{\eta=0}$$

(3.23)

with $p_0 = p_{\eta=0}$. Relations $q = p\sqrt{x}$ and $q = \psi \exp(ik_a\xi)$ give

$$\frac{ik_0}{Z} \psi_0 = \sin a_H \left[\left(\frac{\partial \psi}{\partial \xi}\right)_{\eta=0} + ik_a\psi_0\right] - \frac{1}{\cos a_H} \left(\frac{\partial \psi}{\partial \eta}\right)_{\eta=0}$$

(3.24)

where a term $-\frac{1}{2}\psi_0/\xi$ in the factor in square brackets is neglected and k_0 the wave number at the ground surface.

From Eq. (3.22) expressions for $\psi_0(a)$ and $\psi_0(b)$ will be derived. Using these expressions, the triagonal matrices $\boldsymbol{M_1}$ and $\boldsymbol{M_2}$ given by Eqs. (3.10) will be modified, to take the boundary condition at the ground surface into account. For matrix $\boldsymbol{M_2}$ the expression for $\psi_0(b)$ will be used; for matrix $\boldsymbol{M_1}$ the expression for $\psi_0(a)$ will be used. Analogously, the expression for $\psi_{M+1}(a)$ and $\psi_{M+1}(b)$ will be used to take the boundary condition at the top of the grid into account.

First $\psi_0(b)$ is considered for matrix $\boldsymbol{M_2}$. The first-order finite-difference approximations of the derivatives in Eq. (3.22) are

$$\left(\frac{\partial \psi}{\partial \xi}\right)_{\eta=0} = \frac{1}{\Delta \xi} [\psi_0(b) - \psi_0(a)]$$

(3.25)

21

$$\left(\frac{\partial \psi}{\partial \eta}\right)_{\eta=0} = \frac{1}{\Delta \xi} \left[\psi_1(b) - \psi_0(b)\right]$$

These approximations are centered at $\xi = b - \frac{1}{2}\Delta\xi$ and $\eta = \frac{1}{2}\Delta\eta$, respectively. For second-order approximations, the change of the derivatives over the intervals $\xi = \left[b - \frac{1}{2}\Delta\xi, b\right]$ and $\eta = \left[0, \frac{1}{2}\Delta\eta\right]$ are estimated, respectively, using central-difference approximations of the second derivatives $\partial_\xi^2 \psi$ and $\partial_\eta^2 \psi$, respectively. This gives

$$\left(\frac{\partial \psi}{\partial \xi}\right)_{\eta=0} = \frac{1}{2\Delta\xi} \left[-4\psi_0(a) + 3\psi_0(b) + \psi_0(\bar{a})\right]$$

$$\left(\frac{\partial \psi}{\partial \eta}\right)_{\eta=0} = \frac{1}{2\Delta\eta} \left[4\psi_1(b) - 3\psi_0(b) - \psi_2(b)\right]$$
(3.26)

with $\bar{a} = \alpha - \Delta\xi$. From Eqs. (3.22) and (3.24) the expression for $\psi_0(b)$ is found:

$$\psi_0(b) = u\psi_1(b) + v\psi_2(b) + w\psi_0(a) + y\psi_0(\bar{a})$$
(3.27)

where u, v, w and y are given by

$$u = \frac{4}{d\varepsilon}, v = -\frac{u}{4}, w = \frac{2 \sin a_H}{d \, \Delta\xi}, y = -\frac{w}{4}$$
(3.28)

with

$$\varepsilon = 2\Delta\eta \cos a_H$$
(3.29)

and

$$d = -\frac{ik_0}{Z} + \frac{3}{\varepsilon} + \left(\frac{3/2}{\Delta\xi} + ik_a\right) \sin a_H$$
(3.30)

The normalized ground impedance Z and the elevation angle a_H are evaluated at $\xi = b$ in these expressions.

Next $\psi_0(a)$ is considered for matrix $\boldsymbol{M_1}$. Eq. (3.25) gives directly

$$\psi_0(a) = u\psi_1(a) + v\psi_2(a) + w\psi_0(\bar{a}) + y\psi_0(\bar{\bar{a}})$$
(3.31)

with $\bar{\bar{a}} = a - 2\Delta\xi$; the quantities u, v, w and y are given by Eqs. (3.26) to (3.28), where Z and a_H asre now evaluated at $\xi = a$.

At the top of the gris an analogous boundary condition is applied, with normalized impedance $Z = 1$. Eq. (3.25) gives, by substitutions $\sin a_H \rightarrow -\sin a_H$ and $\cos a_H \rightarrow -\cos a_H$ (from $\boldsymbol{n} \rightarrow -\boldsymbol{n}$), $\Delta\eta \rightarrow -\Delta\eta$, $k_0 \rightarrow k_{M+1}$ and $Z \rightarrow 1$:

$$\psi_{M+1}(b) = u_t\psi_M(b) + v_t\psi_{M-1}(b) + w_t\psi_{M+1}(a) + y_t\psi_{M+1}(\bar{a}) \tag{3.32}$$

where u_t, v_t, w_t and y_t are given by

$$u_t = \frac{4}{d_t\varepsilon_t}, v_t = -\frac{u_t}{4}, w_t = -\frac{2\sin a_H}{d_t\,\Delta\xi}, y_t = -\frac{w_t}{4} \tag{3.33}$$

with

$$\varepsilon_t = 2\Delta\eta\,\cos a_H \tag{3.34}$$

and

$$d_t = -ik_{M+1} + \frac{3}{\varepsilon_t} + \left(\frac{3/2}{\Delta\xi} + ik_a\right)\sin a_H \tag{3.35}$$

The elevation angle a_H of the ground surface is evaluated at $\xi = b$ in these expressions. The expression for $\psi_{M+1}(a)$ follows directly from Eq. (3.30):

$$\psi_{M+1}(a) = u_t\psi_M(a) + v_t\psi_{M-1}(a) + w_t\psi_{M+1}(\bar{a}) + y_t\psi_{M+1}(\bar{\bar{a}}) \tag{3.36}$$

Here the quantities u_t, v_t, w_t and y_t are given by Eqs. (3.31) to (3.33), where a_H is now evaluated at $\xi = a$.

For the implementation of the boundary condition on the GTPE matrices ($Eqs.$ 3.10), the left-hand side $\boldsymbol{M_2}\vec{\psi}(b)$ of Eq. (3.9) is first considered. In the column vector $\boldsymbol{\delta}^2\vec{\psi}(b)$ the term $\psi_0(b)$ is 'missing' in the first element and the term $\psi_{M+1}(b)$ is 'missing' in the last element. In the column vector $\boldsymbol{\delta}\,\vec{\psi}(b)$, the term $-\frac{1}{2}\psi_0(b)$ is 'missing' in the first element and the term $\frac{1}{2}\psi_{M+1}(b)$ is 'missing' in the last element. To correct for the 'missing' terms the use of the boundary conditions (3.25) and (3.30) is made. The result is that the boundary conditions at the ground and the top can be considered in the left-hand side $\boldsymbol{M_2}\vec{\psi}(b)$ of Eq. (3.9) by

- replacing $\boldsymbol{\delta}^2\vec{\psi}(b)$ by $\boldsymbol{T_3}\,\vec{\psi}(b) + \boldsymbol{k_3}$,
- replacing $\boldsymbol{\delta}\,\vec{\psi}(b)$ by $\boldsymbol{T_2}\,\vec{\psi}(b) + \boldsymbol{k_2}$,

where $\boldsymbol{T_3}, \boldsymbol{k_3}, \boldsymbol{T_2}$ and $\boldsymbol{k_2}$ are given by

$$\boldsymbol{T_3} = \begin{pmatrix} -2+u & 1+v & & & & \\ 1 & -2 & 1 & & & \\ & 1 & -2 & 1 & & \\ & & \ddots & \ddots & \ddots & \\ & & & 1 & -2 & 1 \\ & & & & 1+v_t & -2+u_t \end{pmatrix} \tag{3.37}$$

23

$$k_3 = \begin{pmatrix} w\psi_0(a) + y\psi_0(\bar{a}) \\ 0 \\ 0 \\ \vdots \\ 0 \\ w_t\psi_{M+1}(a) + y_t\psi_{M+1}(\bar{a}) \end{pmatrix} \tag{3.38}$$

$$T_2 = \frac{1}{2}\begin{pmatrix} -u & 1-v & & & & \\ 1 & 0 & 1 & & & \\ & 1 & 0 & 1 & & \\ & & \ddots & \ddots & & \ddots \\ & & & -1 & 0 & 1 \\ & & & & -1+v_t & u_t \end{pmatrix} \tag{3.39}$$

$$k_2 = \frac{1}{2}\begin{pmatrix} -w\psi_0(a) - y\psi_0(\bar{a}) \\ 0 \\ 0 \\ \vdots \\ 0 \\ w_t\psi_{M+1}(a) + y_t\psi_{M+1}(\bar{a}) \end{pmatrix} \tag{3.40}$$

The quantities u, v, w, y, u_t, v_t, w_t and y_t in these expressions are evaluated at $\xi = b$. The left-hand side $M_2\vec{\psi}(b)$ of Eq. (3.9) becomes

$$\left(c_3 T_3 + c_2 T_2 + c_1\right)\vec{\psi}(b) + c_3 k_3 + c_2 k_2 \tag{3.41}$$

The approach for the right-hand side $M_1\vec{\psi}(a)$ of Eq. (3.9) is analogous. In the column vector $\delta^2\vec{\psi}(a)$, the term $\psi_0(a)$ is 'missing' in the first element and the term $\psi_{M+1}(a)$ is 'missing' in the last element. In the column vector $\delta\,\vec{\psi}(a)$, the term $-\frac{1}{2}\psi_0(a)$ is 'missing' in the first element and the term $\frac{1}{2}\psi_{M+1}(a)$ is 'missing' in the last element. To correct for the 'missing' terms the use of boundary conditions (3.29) and (3.34) is made. The result is that the boundary conditions at the ground and the top can be taken into account in the right-hand side $M_1\vec{\psi}(a)$ of Eq. (3.9) by

- replacing $\delta^2\vec{\psi}(a)$ by $S_3\,\vec{\psi}(a) + m_3$,
- replacing $\delta\,\vec{\psi}(a)$ by $S_2\,\vec{\psi}(a) + m_2$

The expressions for the matrices S_3 and S_2 are identical to the expressions (3.35) and (3.37) for T_3 and T_2, respectively; the quantities u, v, u_t and v_t in Eqs. (3.35) and (3.37) are now evaluated at $\xi = a$ instead of $\xi = b$. The expressions for the vectors m_3 and m_2 are

$$m_3 = \begin{pmatrix} w\psi_0(\bar{a}) + y\psi_0(\bar{\bar{a}}) \\ 0 \\ 0 \\ \vdots \\ 0 \\ w_t\psi_{M+1}(\bar{a}) + y_t\psi_{M+1}(\bar{\bar{a}}) \end{pmatrix} \tag{3.42}$$

$$m_2 = \frac{1}{2} \begin{pmatrix} -w\psi_0(\bar{a}) - y\psi_0(\bar{\bar{a}}) \\ 0 \\ 0 \\ \vdots \\ 0 \\ w_t\psi_{M+1}(a) + y_t\psi_{M+1}(\bar{a}) \end{pmatrix} \tag{3.43}$$

where w, y, w_t and y_t are evaluated at $\xi = a$. The right-hand side $\boldsymbol{M_1}\,\vec{\psi}(b)$ of Eq. (3.9) becomes

$$(d_3 \boldsymbol{S_3} + d_2 \boldsymbol{S_2} + d_1)\overrightarrow{\psi}(a) + d_3 \boldsymbol{m_3} + d_2 \boldsymbol{m_2} \tag{3.44}$$

Salomons [16] does not mention the incompleteness of the boundary conditions incorporation in the GTPE method. Special treatment is needed for the first two nodes of the computational grid in the range direction (ξ) when considering calculation of boundary conditions at top and ground boundaries. As it was shown in Eqs. (3.31) and (3.36), in order to calculate $\psi_0(a)$ the values of $\psi_0(\bar{a})$ and $\psi_0(\bar{\bar{a}})$ should be known (the same applies to $\psi_{M+1}(a)$). In the first range step $\left(i = 1,\ \vec{\psi}(\xi_1)\right)$ both $\bar{a}$ and $\bar{\bar{a}}$ are outside of the grid while in the second range step $\left(i = 2,\ \vec{\psi}(\xi_2)\right)$ $\bar{a}$ exist while $\bar{\bar{a}}$ does not. To overcome this challenge, the axisymmetric nature of the method has been incorporated along with alternative finite-difference approximations of the derivatives in Eq. (3.24).

For the method to be axisymmetric, the relation $\left(\frac{\partial\psi}{\partial\xi}\right)_{\xi=0,i=0} = 0$ should be true for every η in the vertical direction. Using central finite-difference approximation for this derivative centered at $\xi = 0, i = 0$, over the interval $\xi = [-\Delta\xi, \Delta\xi]$, for every η in the vertical direction:

$$\frac{\psi(\Delta\xi)-\psi(-\Delta\xi)}{2\Delta\xi} = 0 \Rightarrow \psi(\Delta\xi) = \psi(-\Delta\xi) \tag{3.45}$$

Now, using backwards finite-difference approximation for the same derivative centered at $\xi = \Delta\xi, i = 1$ over the interval $\xi = [-\Delta\xi, \Delta\xi]$, for every η in the vertical direction:

$$\left(\frac{\partial\psi}{\partial\xi}\right)_{\xi=\Delta\xi,i=1} = \frac{\psi(\Delta\xi) - \psi(-\Delta\xi)}{\Delta\xi} = 0 \tag{3.46}$$

With Eq. (3.46) for the derivative in ξ direction and Eq. (3.26) for the η derivative, boundary conditions $\psi_1(a)$ and $\psi_{M+1}(a)$ for the first range step ($\xi = \Delta\xi, i = 1$) can be calculated from Eq. (3.24):

$$\psi_0(a) = \left[-\frac{2}{\Delta\eta \cos a_H}\psi_1(a) + \frac{1}{2\Delta\eta \cos a_H}\psi_2(a)\right]\Big/\left[\frac{ik_0}{Z} - \sin a_H\, ik_a - \frac{3}{2\Delta\eta \cos a_H}\right] \tag{3.47}$$

$$\psi_{M+1}(a) = \left[-\frac{2}{\Delta\eta \cos a_H}\psi_M(a) + \frac{1}{2\Delta\eta \cos a_H}\psi_{M-1}(a)\right]\Big/\left[ik_{M+1} + \sin a_H\, ik_a + \frac{3}{2\Delta\eta \cos a_H}\right] \tag{3.48}$$

The quantity a_H and Z in Eqs. (3.47) and (3.48) is evaluated at $\xi = a$.

Additionally, for the second range step ($\xi = 2\Delta\xi, i = 2$), Eq. (3.26) is used for the η derivative while for the derivative in the ξ direction first order backwards finite-difference approximation is used for every η in the vertical direction:

$$\left(\frac{\partial\psi}{\partial\xi}\right)_{\xi=b} = \frac{\psi(b) - \psi(a)}{\Delta\xi} \tag{3.49}$$

This approximation is centered at $\xi = b$ over the interval $\xi = [a, b = a + \Delta\xi]$. Finally, from Eq. (3.24), using Eqs. (3.26) and (3.49) boundary conditions for ground and top boundaries in the second range step can be calculated:

$$
\psi_0(b)
$$
$$
= \left[\begin{array}{c} -\dfrac{\sin a_H}{\Delta\xi}\psi_0(a) - \dfrac{2}{\Delta\eta\,\cos a_H}\psi_1(b) + \\[2mm] \dfrac{1}{2\Delta\eta\,\cos a_H}\psi_2(b) \end{array}\right] \left[\begin{array}{c} \dfrac{ik_0}{Z} - \sin a_H\,ik_a - \dfrac{\sin a_H}{\Delta\xi} \\[2mm] -\dfrac{3}{2\Delta\eta\,\cos a_H} \end{array}\right]^{-1} \tag{3.50}
$$

$$
\psi_{M+1}(b)
$$
$$
= \left[\begin{array}{c} \dfrac{\sin a_H}{\Delta\xi}\psi_{M+1}(a) - \dfrac{2}{\Delta\eta\,\cos a_H}\psi_M(b) + \\[2mm] \dfrac{1}{2\Delta\eta\,\cos a_H}\psi_{M-1}(b) \end{array}\right] \left[\begin{array}{c} ik_{M+1} + \sin a_H\,ik_a + \dfrac{\sin a_H}{\Delta\xi} \\[2mm] -\dfrac{3}{2\Delta\eta\,\cos a_H} \end{array}\right]^{-1} \tag{3.51}
$$

The quantity a_H and Z in Eqs. (3.47) and (3.48) is evaluated at $\xi = b$.

The same applies for boundary conditions on $\xi = a$, with b being replaced by a and a by $\bar{a}$, with a_H and Z evaluated at $\xi = a$.

The impedance at the top surface ($Z = 1$) only allows vertical traveling plane waves to pass through without any reflection. However, other types of waves experience partial reflection back into the region $\eta < \eta_M$. To eliminate these reflections, an absorbing layer is placed just below the top surface, between $\eta = \eta_t$ and $\eta = \eta_M$ as shown in Fig. 3. Within this absorbing layer, an imaginary term is introduced into the wave number $k(\eta)$ for $\eta_t \le \eta \le \eta_M$ in order to gradually attenuate the waves. Numerical tests have demonstrated that a suitable choice for the imaginary term is $iA_t\,(\eta - \eta_t)^2/(\eta_M - \eta_t)^2$, where A_t represents a constant. The optimal selection for A_t depends on the frequency. For frequencies $1000, 500, 125$ and $30\,Hz$ it is recommended to use $A_t = 1, 0.5, 0.4, 0.2$ respectively, while interpolation is employed for intermediate frequencies.

The definition of the wave number is

$$k(\eta) = \frac{\omega}{c_{eff}} \tag{3.52}$$

with ω being the angular frequency and c_{eff} the effective sound speed, defined as

$$c_{eff}(\eta) = c_o + b \, ln\left(1 + \frac{\eta}{\eta_o}\right) \tag{3.53}$$

with c_o being the sound speed on the ground surface, b the refraction factor and η_o the roughness length of the ground.
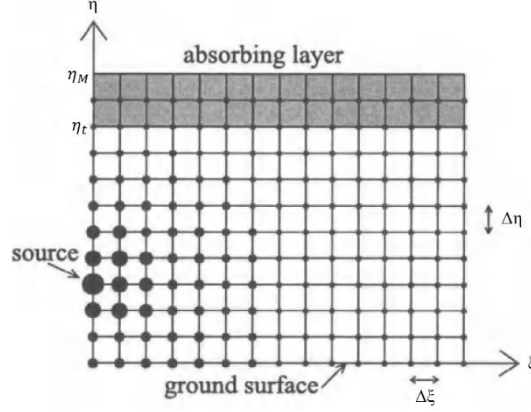
Figure 3: Grid in the $\xi\eta$ plane with an absorbing layer at the top.

As [16] suggests and [25] proves, the thickness of the absorption layer should be at least $50 \cdot \lambda$ wide in order to have a converging and realistic solution.

Furthermore, in [25] it was shown that a uniform and equidistant numerical grid with spacing $\Delta\xi = \Delta\eta = \lambda/10$ sufficient is accurate and stable at the same time. These values will be used in the rest of this work.

3.3 Absorption losses

The following section will be developed according to [25]. The amplitude of the complex pressure undergoes an exponential decrease due to atmospheric absorption. To incorporate this effect, a small imaginary term $i \cdot k_i$ is added to the wave number. This results in the replacement of k with $k + ik_i$.

The term k_i is defined as

$$k_i = \frac{a}{20 \, loge} \tag{3.54}$$

with a being the absorbing coefficient, determined by the relationship

$$a = 8.686f^2\sqrt{\tau_r}\left(\frac{1.84}{10^{11}\rho_r} + \frac{b_1 + b_2}{\tau_r^3}\right) \tag{3.55}$$

where $\tau_r = T/T_{20}$, $T_{20} = 293.15K$ and $\rho_r = p_a/p_r$, $p_r = 101325Pa$. The terms b_1 and b_2 are defined as

$$b_1 = 0.1068 \frac{e^{-3352/T}}{f_{r,N} + f^2/f_{r,N}} \tag{3.56}$$

$$b_2 = 0.01275 \frac{e^{-2239.1/T}}{f_{r,O} + f^2/f_{r,O}} \tag{3.57}$$

with $f_{r,N}$ and $f_{r,O}$ being the relaxation frequencies on nitrogen and oxygen, calculated from the relationships

$$f_{r,N} = \frac{\rho_r}{\sqrt{\tau_r}} \left[9 + 280h \, e^{-4.17\left(1/\sqrt[3]{\tau_r}-1\right)} \right] \tag{3.58}$$

$$f_{r,O} = \rho_r \left(24 + 40400h \frac{0.02 + h}{0.0391 + h} \right) \tag{3.59}$$

In the above expressions h is the percentage of molar water vapor concentration in the atmosphere and is a function of the relative humidity r_h, which is defined as the percentage of the water vapor pressure in the atmosphere over the saturation pressure p_{sat}

$$h = \frac{r_h \, \rho_{sat}}{\rho_r} \tag{3.60}$$

where $\rho_{sat} = p_{sat}/p_r$ and is calculated by from the relation $\rho_{sat} = 10^{C_{sat}}$, with

$$C_{sat} = -6.8346 \left(\frac{T_{01}}{T} \right)^{1.261} + 4.6151 \tag{3.61}$$

where $T_{01} = 273.15$ is the triple point temperature of water.

3.4 Simulation of the acoustic source

Having defined the boundary conditions, the initial condition of the PE needs to be defined as well. This is done through the acoustic source at the start of the numerical grid i.e., first range step ($\xi = \Delta\xi$, $i = 1$). The relationships below will be given in the physical domain (r, z) but can easily be transformed to the computational domain (ξ, η).

The exact solution for the field of a monopole source in an unbounded, non-refractive atmosphere is

$$q(r,z) = \frac{e^{ikR}}{R} \sqrt{r} \tag{3.62}$$

where R is the distance from the source.

Although this formula is theoretically correct, in reality it becomes infinite at the source, thus being unsuitable for numerical studies. Instead, the following starting field will be used

$$q(0, z) = q_0(z - z_s) + C\, q_0(z + z_s) \tag{3.63}$$

with the source positioned at $(r, z) = (0, z_s)$.

The reflection coefficient C is calculated via the expression

$$C = \frac{Z - 1}{Z + 1} \tag{3.64}$$

where Z is the normalized ground impedance.

The function $q_0(z)$ in Eq. (3.63) is defined as

$$q_0(0, z) = \sqrt{ik_0}(1.3717 - 0.3701 k_a^2 z^2) e^{-k_a^2 z^2 / 3} \tag{3.65}$$

In Eqs. (3.63) and (3.65) q can be replaced by ψ using the Equation (2.6).

4. Application and results

This chapter is divided into two sections. In the first section the developed GTPE model is applied on sound propagation over hills in non-turbulent atmosphere, and the results are compared with other predictions. In the second section, the developed model is applied on sound propagation in turbulent atmosphere. Results are compared against predictions from other models in flat terrain.

4.1 Sound propagation over irregular terrain in non-turbulent atmosphere

4.1.1 Comparison with predictions from R.A. Sack & M. West

In this subsection, the results of the developed model are compared against the predictions of the GTPE model as initially formulated by R.A. Sack & M. West [21]. It should be noted that the two methods are the same; so differences in the predictions may arise either from differences in the grid density or from differences in ground, wind velocity and source modeling which is not strictly mentioned in [21]. The following parameter values have been used in the simulation:

- Source position: $(r_s, z_s) = (0,2)\ [m]$
- Receiver position: $(r_r, z_r) = (0{\sim}2600,2)\ [m]$
- Absorption layer thickness: 50λ
- Absolute temperature: $T = 293.15K$
- Relative humidity: $r_h = 70\%$
- Reference speed of sound: $c_0 = \sqrt{\gamma RT} = 343.2\ [m/s]$
- Ground roughness length: $z_0 = 0.1\ [m]$
- Frequency $f = 50Hz$

The hill is described by the following expression

$$H(x) = a\ cos^2\left[\frac{\pi s}{2}\left(1 - \frac{x}{x_{top}}\right)\right], s = \frac{2x_{top}}{W} \tag{4.1}$$

for $W/2 \leq x \leq 3W/2$ and elsewhere $H(x) = 0$. The height of the hill is set to $a = 200m$, which is the value of $H(x)$ when $x = x_{top} = 1000m$ and $W = 1000m$ is the width of the base of the hill. It should be noted that the maximum slope in this hill case is 32.14^o, a value slightly above the recommended limit of 30 degrees.

The ground is assumed rigid, so a very large value of flow resistivity is used to simulate infinity $(\sigma = 10^{20}\ [Pa \cdot s/m^2])$. The normalized ground impedance is given by the expression

$$Z = 1 + 9.08 \left(1000\frac{f}{\sigma}\right)^{-0.75} + i\ 11.9 \left(1000\frac{f}{\sigma}\right)^{-0.73} \tag{4.2}$$

The quantity used for comparison is the relative sound pressure level (or attenuation) given by the expression:

$$\Delta L = 10\ log\left(\frac{|p_c|^2}{|p_{free}|^2}\right) \tag{4.3}$$

where $|p_c|$ is the amplitude of the complex pressure and $|p_{free}|$ is the amplitude of the free field pressure at the distance of $100m$.

The free field is the sound field of the source in an unbounded, homogeneous atmosphere and it is expressed as

$$p_{free} = \frac{e^{ik_0 R}}{R} \tag{4.4}$$

with R being the distance from the source.

Comparison is made for two cases: In the first a quiescent medium is considered (zero wind velocity), whilst in the second a constant logarithmic profile is assumed over the hilly terrain. For the case with logarithmic wind profile, the refraction factor is equal to $b = 2.17[m/s]$, accounting for downwind propagation, with wind velocity of $10m/s$ at the height of $10m$.
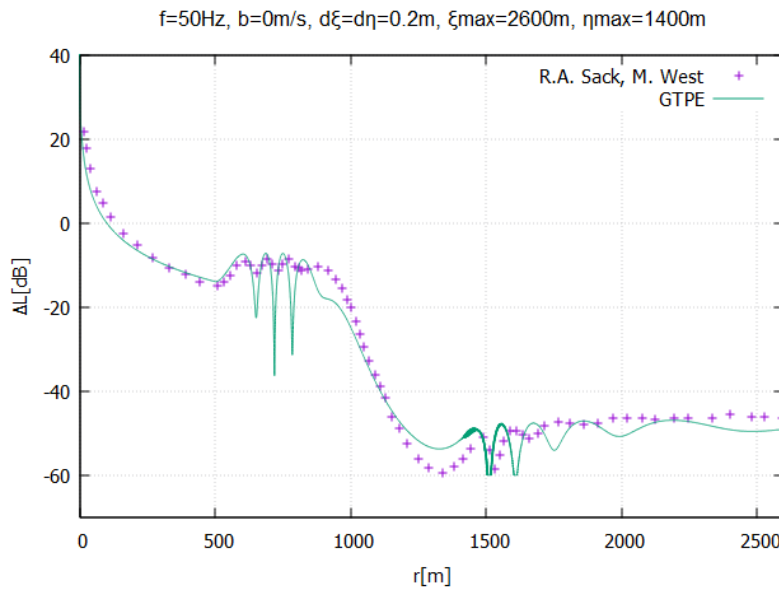
Figure 4: Relative sound pressure level ΔL (attenuation) versus range for still air conditions. The results from the developed GTPE model are compared with those from R.A. Sack & M. West [21].

f=50Hz, b=2.17m/s, dξ=dη=0.2m, ξmax=2600m, ηmax=1400m
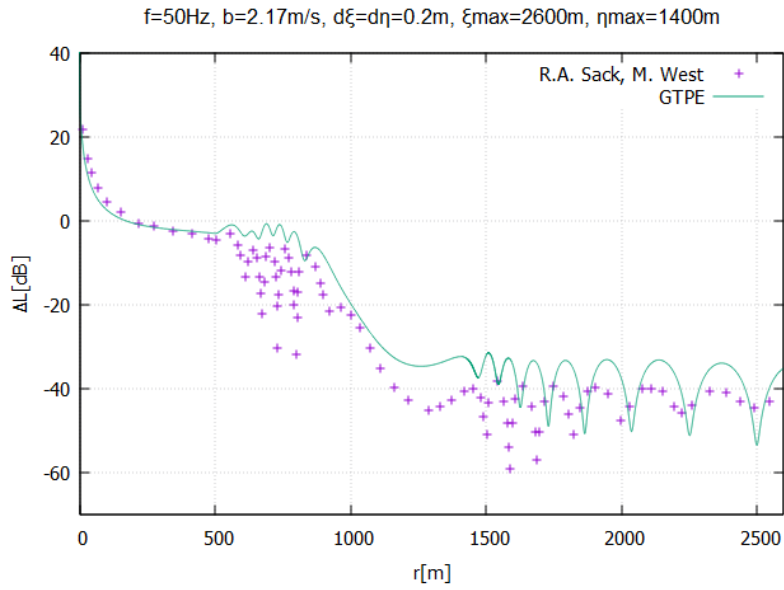
Figure 5: Relative sound pressure level ΔL (attenuation) versus range with a logarithmic wind speed profile. The results from the developed GTPE model are compared with those from R.A. Sack & M. West [21].

Fig. 4 refers to the case of still air conditions. The agreement between the two models is good. The predictions of the present model exhibit more extensive fluctuations in the front side of the hill, indicating that the small grid step of $0.2m$ that was used offered a more detailed result. On the other hand, the case with the logarithmic wind velocity (Fig. 5) shows exactly the opposite behavior. Several factors could attribute to these differences, including a different speed profile, different normalized acoustic impedance or even different source expression. However, the same trend of fluctuating attenuations is predicted from both models downstream of the hill.

f=50Hz, b=0m/s, dξ=dη=0.2m, ξmax=2600m, ηmax=1400m
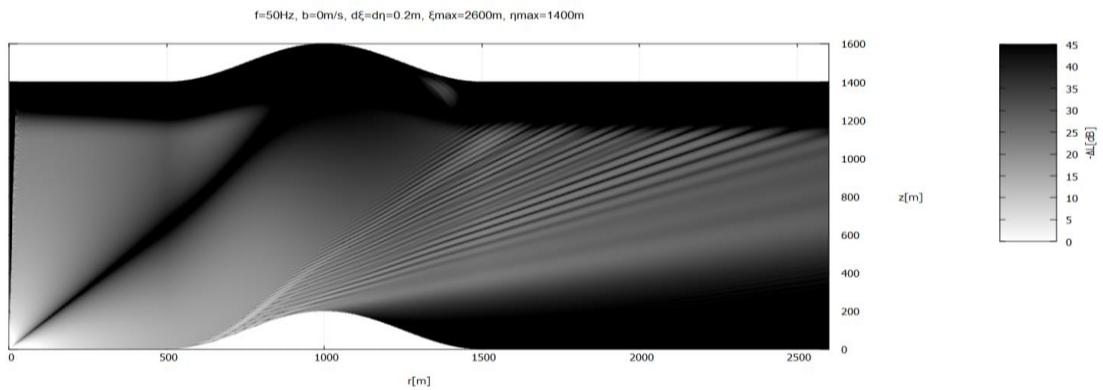
Figure 6: Contour of the opposite of relative sound pressure level -ΔL in same conditions as Fig. 4.
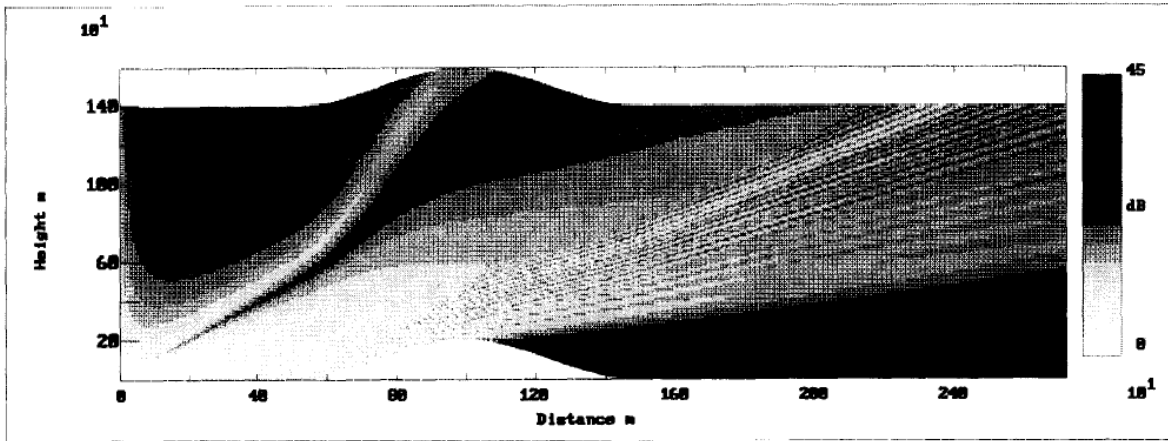
Figure 7: Contour of the opposite of relative sound pressure level -ΔL in same conditions as Fig. 4 predicted by R.A. Sack & M. West [21].

Figures 6 and 7, representing the *ΔL* contours are compared qualitatively. In both figures the shadow zone, i.e. the area were the sound waves fail to propagate is present. Furthermore there is a clear indication in both figures that a large number of sound waves are concentrated in the area in front of the hill, creating elevated levels of sound pressure level in the area. This is caused by reflections that take place in that part of the hill, due to the inclined terrain.

The assumption of a constant logarithmic wind velocity profile, despite being realistic for flat terrain cases, deviated significantly from reality when large elevation and complex terrain are present. In order to assess the effect of a more realistic wind velocity file on sound propagation the simulation is repeated using the flowfield predicted by the incompressible Navier-Stokes solver OpenFOAM. [REF].
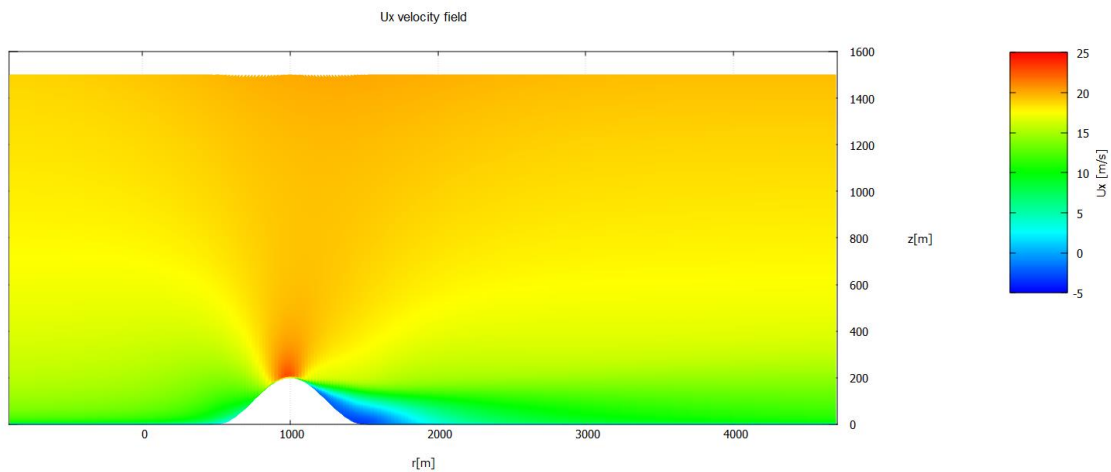
Figure 8: Contours of the axial component of the velocity for the hill of the R.A. Sack & M. West case.

33
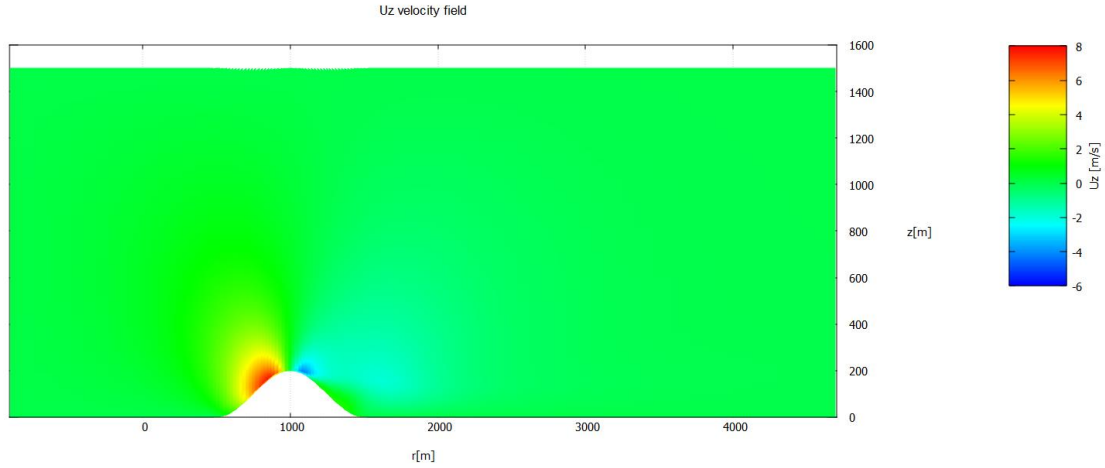
Figure 9: Contours of the vertical component of the velocity for the hill of the R.A. Sack & M. West case.
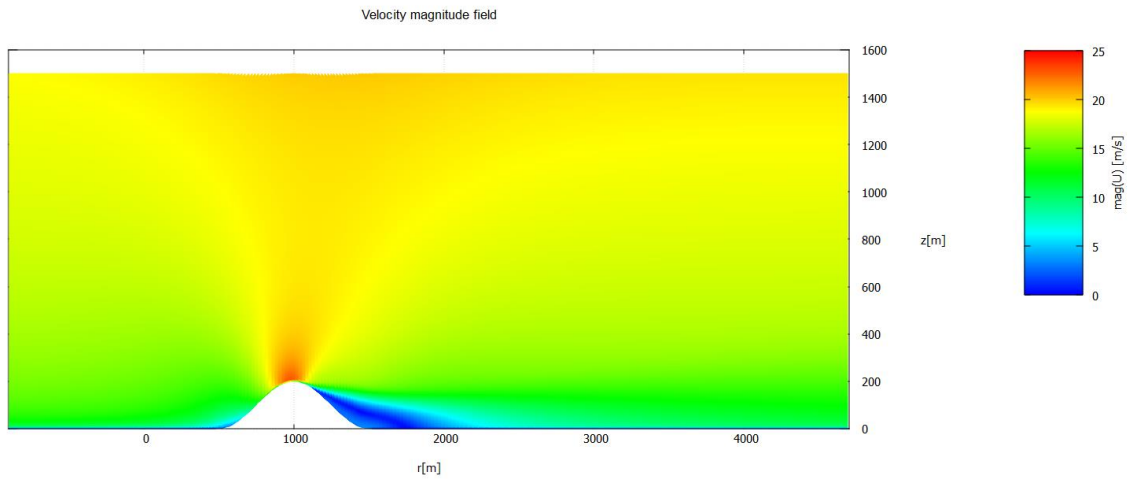
Figure 10: Contours of the velocity modulus for the hill of the R.A. Sack & M. West case.

For these CFD simulations the constant logarithmic wind speed profile used in the previous simulation was imposed at the inlet. Figures 8 and 9 depict the contours of the predicted wind velocity components, whilst Figure 10 depicts the contours of the wind velocity modulus. The flow decelerated upwind of the hill, strongly accelerates on the hill top and then exhibits a strong deceleration in the lee side of the hill. Figure 8 demonstrates that there is a recirculation zone in this region. Regarding the contribution of the wind velocity to the effective sound speed there are two options: The first is to include only the axial component meaning that the effective sound speed is given by

$$c_{eff}(\xi, \eta) = c_o + U_x \qquad (4.5)$$

The second is to include the velocity modulus meaning that the effective sound speed is given by

$$c_{eff}(\xi,\eta) = c_o + \sqrt{U_x^2 + U_z^2}$$

<div align="right">(4.6)</div>

The first option ignores the effect of the vertical component whilst the second ignores the effect of the negative velocity in the recirculation zone.

In Figure 11 the ΔL predictions using a constant logarithmic profile (presented also in Fig. 5) are compared with those obtained when the effective sound speed is calculated using Eq. (4.5), whilst in Figure 12 the same comparison is made when the effective sound speed is calculated using Eq. (4.6). For completeness the predictions of Sack and West for the constant logarithmic profile are depicted in the figures. In both cases a reduction of the sound attenuation is observed when a more accurate wind velocity profile is employed. This is due to the flow acceleration on the hilltop which results in a stronger downward refraction of the sound waves, thus increasing the sound pressure level. Figure 13 focuses on the comparison between the two different ways of calculating the effective sound speed. Differences are observed only downstream of the hill top due to the fact that the axial component of the wind velocity deviates more from the velocity modulus in this region. Usage of Eq. (4.6) causes fluctuations with larger amplitudes and a slightly larger mean attenuation value.
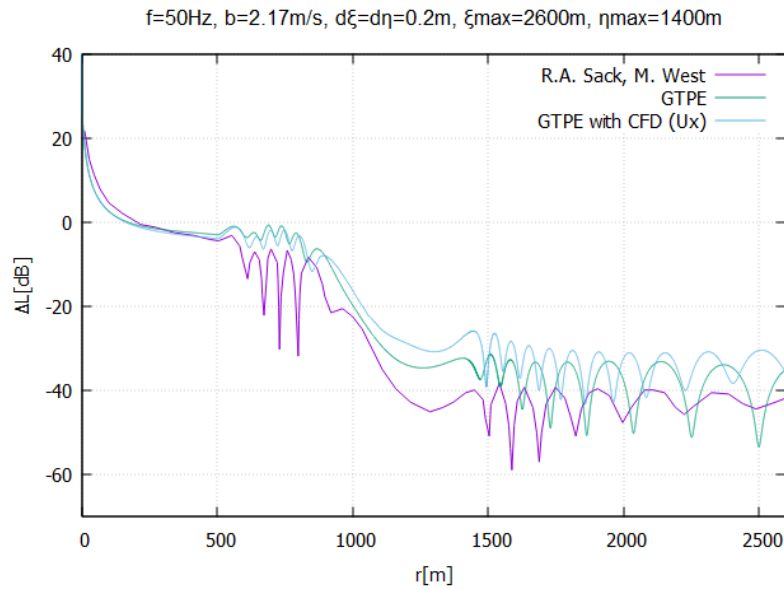
Figure 11: Predictions of the relative sound pressure level ΔL (attenuation) versus range using the developed GTPE model. Green curve: Results correspond to a constant logarithmic wind velocity profile. Light blue curve: Results including the axial component of the wind velocity as obtained by CFD (Eq. 4.5). The results of Sack and West [21] are included for completeness.
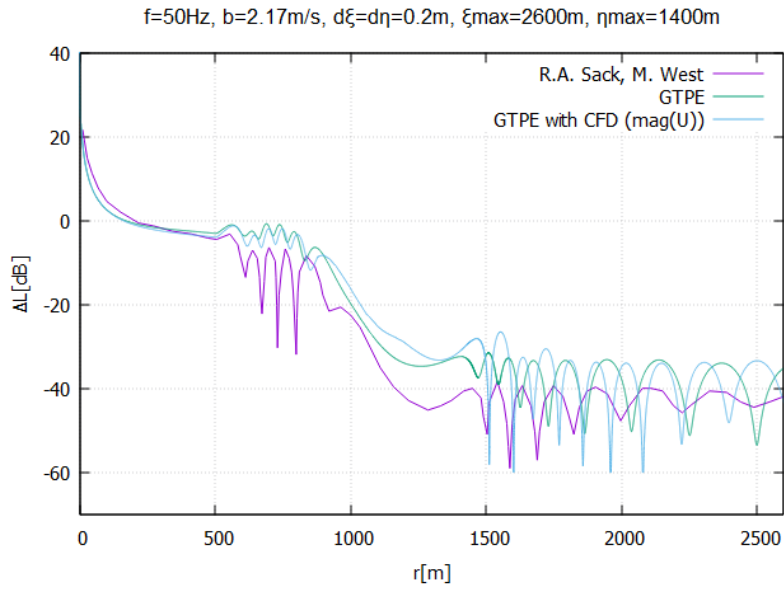
Figure 12: Predictions of the relative sound pressure level ΔL (attenuation) versus range using the developed GTPE model. Green curve: Results correspond to a constant logarithmic wind velocity profile. Light blue curve: Results including the wind velocity modulus as obtained by CFD (Eq. 4.6). The results of Sack and West [21] are included for completeness.
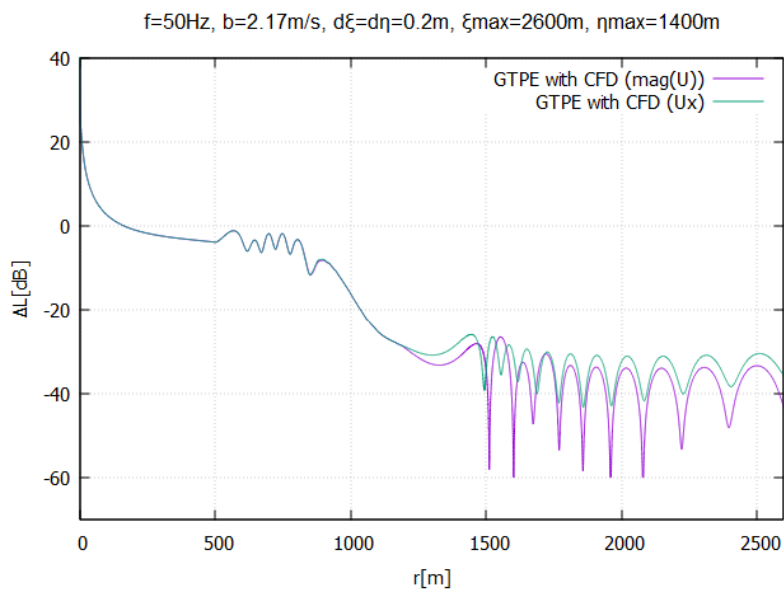

Figure 13: Relative sound pressure level ΔL (attenuation) against the r-range under downwind propagation from the GTPE model using CFD data. The two cases differ in the way that the effective sound speed is calculated.

4.1.2 Comparison with predictions from E.M. Salomons

In this sub-section the results of the developed GTPE model are compared with the GTPE predictions presented by E.M. Salomons [16, Chapter 6]. The following parameter values are used for the simulation:

- Source position: $(r_s, z_s) = (0,2) \, [m]$
- Receiver position: $(r_r, z_r) = (0{\sim}1000,2) \, [m]$
- Absorption layer thickness: 50λ
- Absolute temperature: $T = 293.15K$
- Relative humidity: $r_h = 70\%$
- Reference speed of sound: $c_0 = \sqrt{\gamma RT} = 343.2 \, [m/s]$
- Ground roughness length: $z_0 = 0.1 \, [m]$
- Frequency $f = 300Hz \, \& \, 500Hz$
- Flow resistivity $\sigma = 2 \cdot 10^5 \, [Pa \cdot s/m^2]$

The hill is described by the following expression, given in [33]. In this case the hill has a height of $H = 10m$ and a base length of $W = 250m$, starting from $x_o = 50m$ so the top is at $x_{top} = 175m$. It is composed of three circular arcs with radius $R = H/4 + W^2/16H$

$$for \; x \in (x_o, x_o + 0.25W), \quad H(x) = R - \sqrt{R^2 - (x - x_o)^2}$$

$$for \; x \in (x_o + 0.25, x_o + 0.75W), \quad H(x) = H - R + \sqrt{R^2 - \left(x - x_{top}\right)^2} \qquad (4.7)$$

$$for \; x \in (x_o + 0.75, x_o + W), \quad H(x) = R - \sqrt{R^2 - (x - x_o + W)^2}$$

and elsewhere $H(x) = 0$.

Here, the flow resistivity is not infinite (porous ground), so the normalized ground impedance takes the value of $Z = 7.7 + 8.85i$ for 300Hz and $Z = 5.57 + 6.1i$ for 500Hz.

The quantity used for comparison of each predictions was the relative sound pressure level (or attenuation) given by the expression (4.3). In this case thought, $\left|p_{free}\right|$ is the amplitude of the free field pressure at distance $R = \sqrt{(z - z_s)^2 + r^2}$.

For the case with logarithmic wind profile, the refraction factor is equal to $b = 1[m/s]$, accounting for downwind propagation.
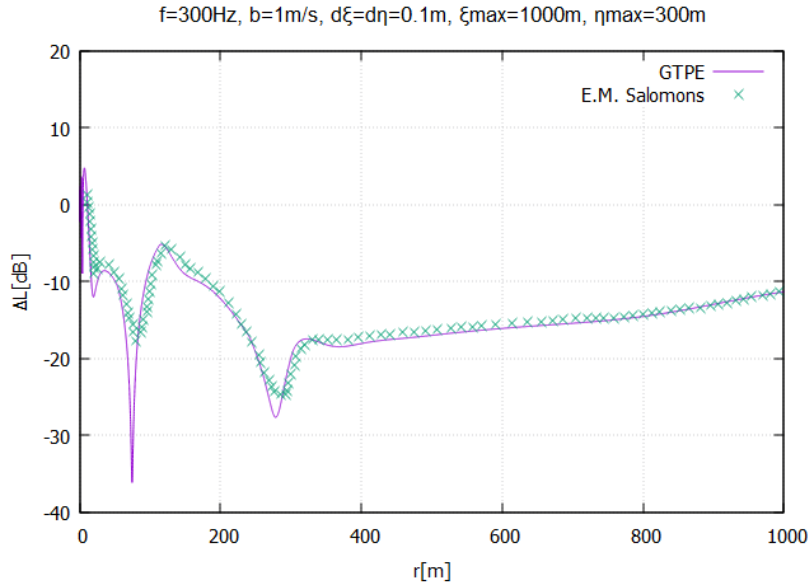
Figure 14: Relative sound pressure level ΔL (attenuation) versus range under downwind sound propagation. The results from the developed GTPE model are compared with those from E.M. Salomons [16].

Good agreement is found between the results from the present model and those from E.M. Salomons. The main difference that is presented here is the depth of the "dip" that occurs at approximately 75m. This could be the result of a smaller grid step used in the GTPE model, which makes it capable of detecting such steep changes in the value of the relative sound pressure level as observed here.

In the following cases, the same simulation parameters and the same hill geometry are kept, but the size and the position of the hill with respect to the source are altered. The hill now presents its peak at $x_{top} = 375m$ and has a base length of $W = 500m$. Two simulations are performed, one for still air and another for downwind propagation conditions, and the ΔL contours are compared with the corresponding given by Salomons.
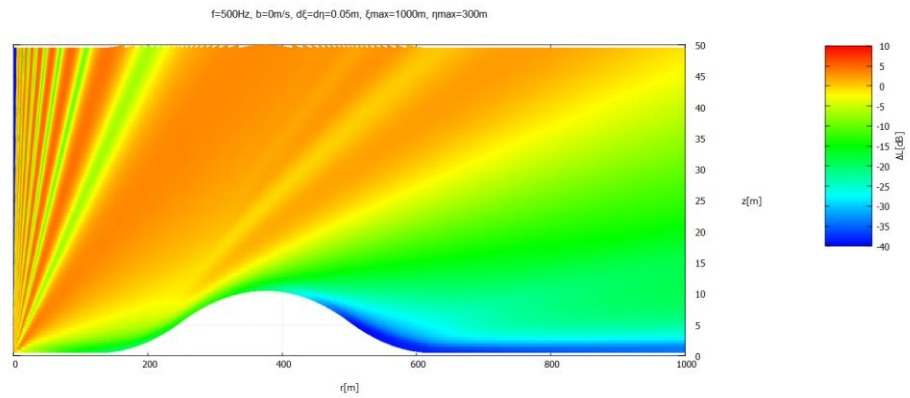
Figure 15: Contours of relative sound pressure level ΔL (attenuation) under still air conditions, results from the GTPE model.
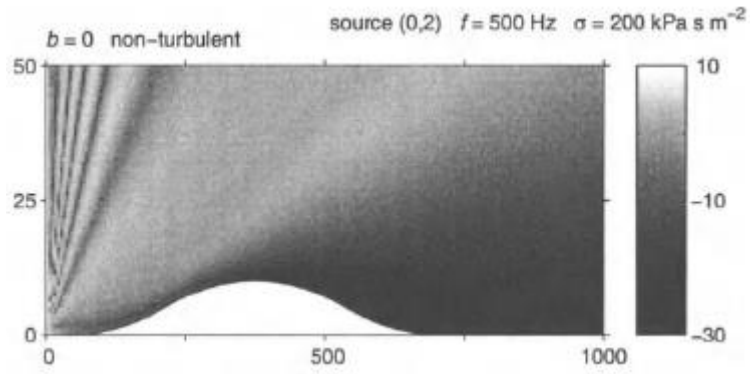
Figure 16: Contours of relative sound pressure level ΔL (attenuation) still air conditions, results from E.M. Salomons [16].
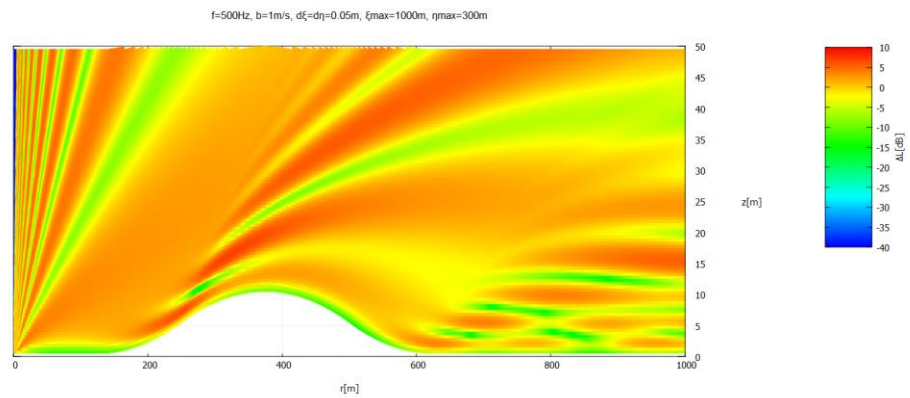
Figure 17: Contours of relative sound pressure level ΔL (attenuation) under downwind wind propagation, results from the GTPE model.
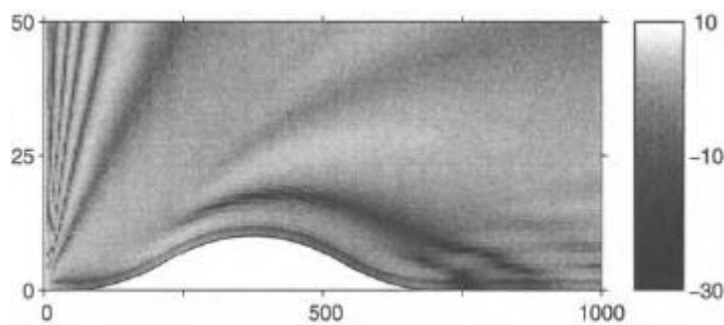

Figure 18: Contours of relative sound pressure level ΔL (attenuation) under downwind wind propagation, results from E.M. Salomons [16].

Figures 15 and 16 but also Figures 17 and 18 present good qualitative agreement with each other. In the non-moving medium cases (Fig. 15 & 16) the area of the acoustic shadow zone is easily observed. In the other two figures such a shadow zone does not exist. This is an expected result, as the logarithmic wind profile refracts the sound waves downwards and subsequently the sound travels to regions that are not visible from the position of the source.

As in the cases studied in chapter 4.1.1, the velocity field for the downwind propagation case of Figure 14 is also calculated using the Navier-Stokes solver OpenFOAM.
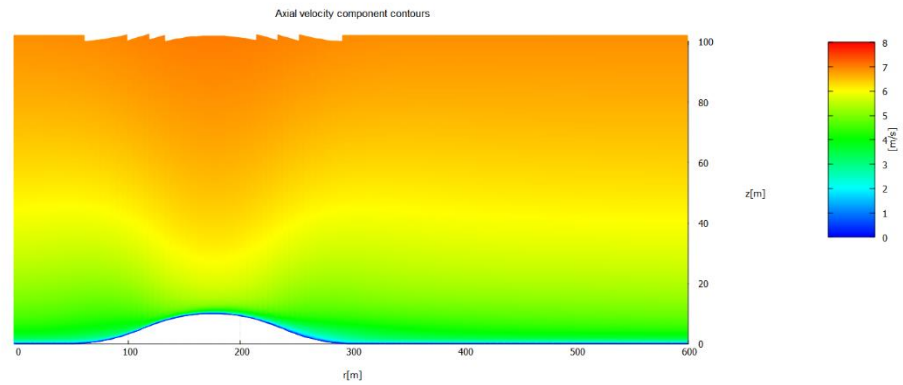
Figure 19: Contours of the axial component of the velocity for the hill of the E.M. Salomons case.
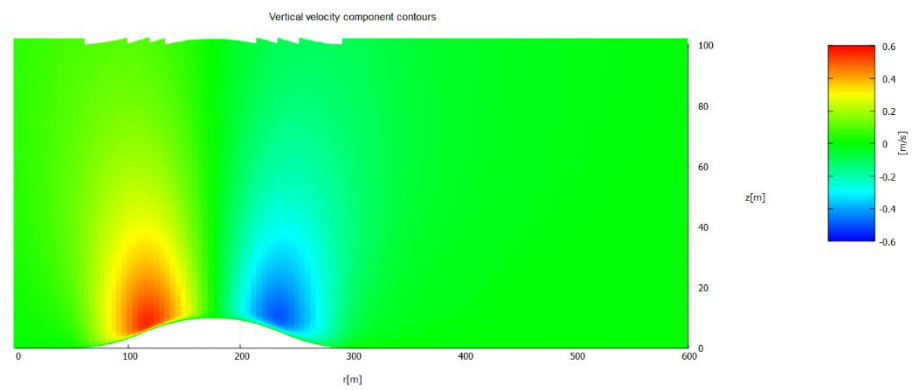

Figure 20: Contours of the vertical component of the velocity for the hill of the E.M. Salomons case.
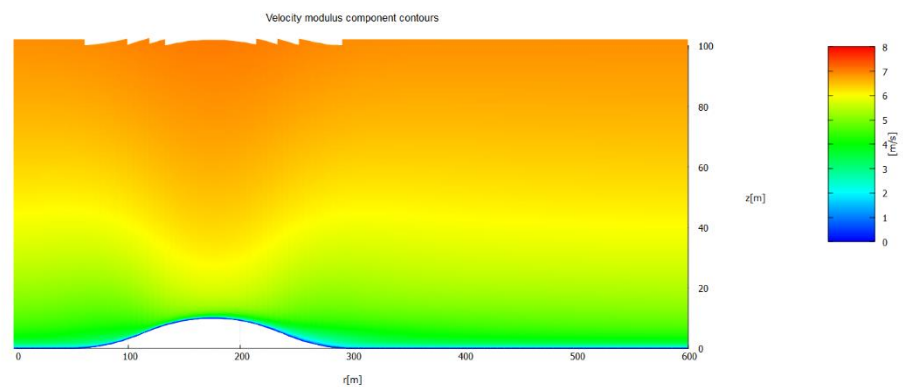

Figure 21: Contours of the velocity modulus for the hill of the R.A. Sack & M. West case.

Figures 19 and 20 represent the contours of the axial and vertical components of the velocity respectively, whilst Figure 21 represents the contours of the velocity modulus. Figures 19 and 21 are indistinguishable. This fact can be attributed to the absence of recirculation in the area after the hill and thus the existence of only positive values for the velocity field of the axial component. The contribution of the vertical component in the magnitude is quite small, so the similarity of the two figures is expected.
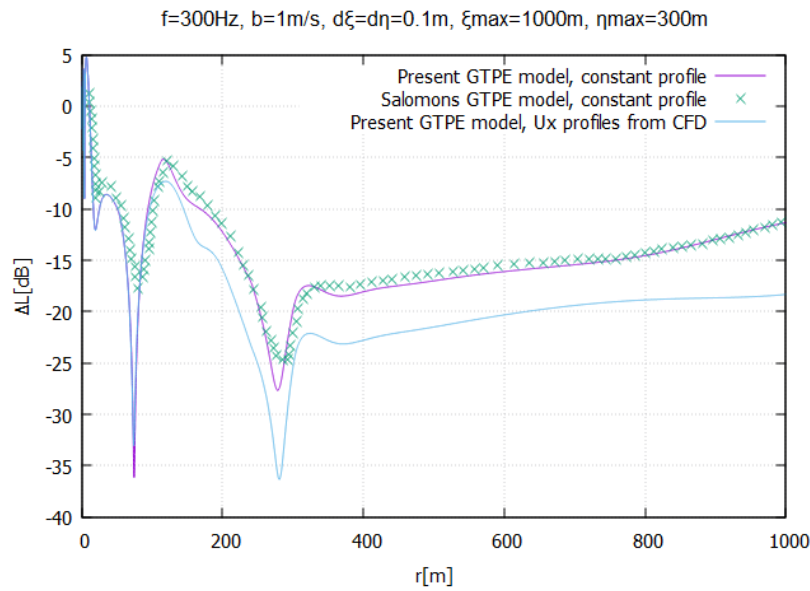
Figure 22: Predictions of the relative sound pressure level ΔL (attenuation) versus range using the developed GTPE model. Purple curve: Results correspond to a constant logarithmic wind velocity profile. Light blue curve: Results including the axial component of the wind velocity as obtained by CFD (Eq. 4.5). The results of E.M. Salomons [16] are included for completeness.
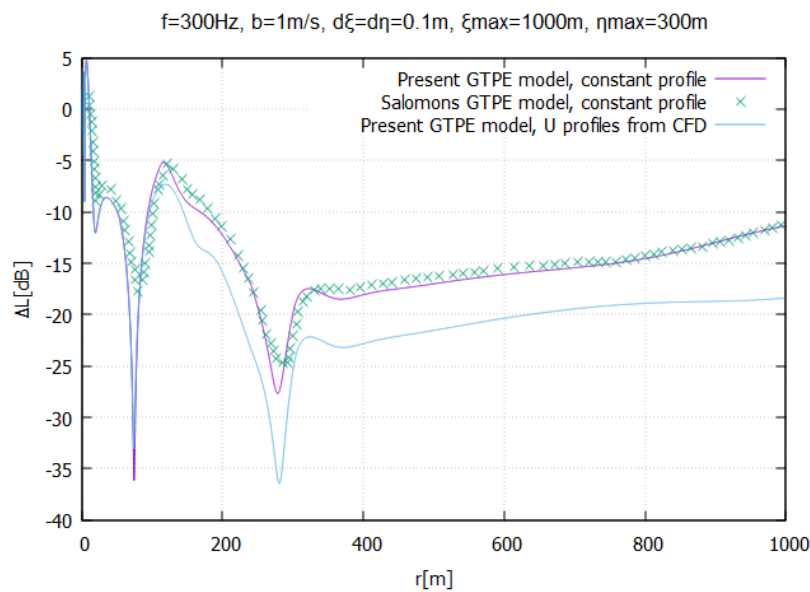

Figure 23: Predictions of the relative sound pressure level ΔL (attenuation) versus range using the developed GTPE model. Purple curve: Results correspond to a constant logarithmic wind velocity profile. Light blue curve: Results including the wind velocity modulus as obtained by CFD (Eq. 4.6). The results of E.M. Salomons [16] are included for completeness.

In this case, the effect of the CFD data is the deeper "dip" after the hill along with lower values of ΔL after the peak at 175m in general.

Contrary to Figures 11,12 which refer to the steepest hill used by Sack and West, in Figures 22, 33 it is observed that the effect of the more realistic velocity field is to increase sound attenuation. This is due to the fact that the flow acceleration on the hill top is less and does not cause a strong refraction of the sound waves downwards. In this case sound propagation is more affected by the flow deceleration upstream and downstream of the hill. The velocity magnitude is reduced and has a weaker favorable effect to sound propagation.

4.1.3 Comparison with predictions from Ray Theory

In this sub-section results from the GTPE method are compared with the predictions of a ray tracing model, developed by Prospathopoulos and Voutsinas [34]. The hill shape is given by Eq. (4.7) and the simulation parameter take the following values:

- Source position: $(r_s, z_s) = (0,5)\ [m]$
- Receiver position: $(r_s, z_s) = (0\sim500,2)\ [m]$
- Absolute temperature: $T = 293.15K$
- Relative humidity: $r_h = 70\%$
- Reference speed of sound: $c_0 = \sqrt{\gamma R T} = 343.2\ [m/s]$
- Ground roughness length: $z_0 = 0.03\ [m]$
- Frequency $f = 250Hz$
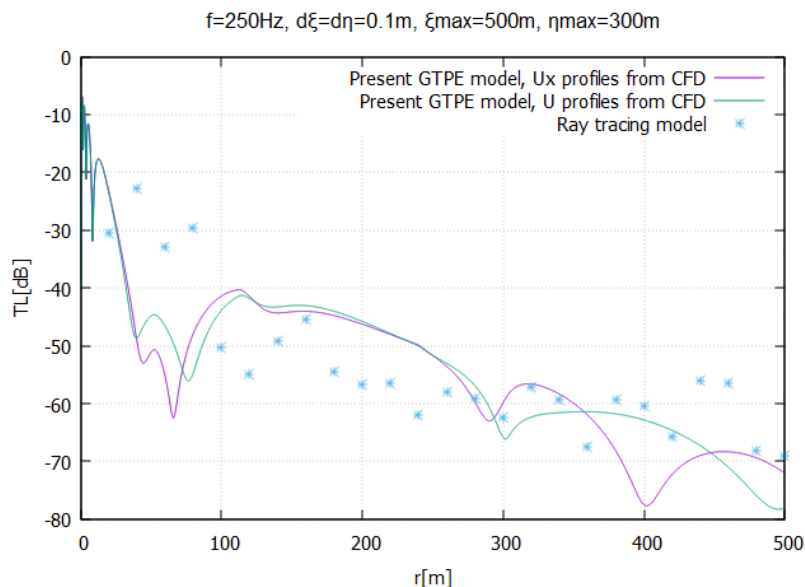- Flow resistivity $\sigma = 3.6 \cdot 10^5\ [Pa \cdot s/m^2]$

Figure 24: Predictions of the transmission loss (TL) versus range using the developed GTPE model. Purple curve: Results including the wind velocity modulus as obtained by CFD (Eq. 4.6). Green curve: Results including the axial component of the wind velocity as obtained by CFD (Eq. 4.5). Light blue points: Results from Ray tracing model [33]

In the ray tracing model, the wind velocity is added in a vectorial way to the sound speed. In this way, both axial and vertical components of the velocity field predicted using the OpenFOAM solver are taken into account. On the other hand, ray tracing is a geometrical approximation based on the accurate determination of eigenrays. This methodology has been proven sensitive to overestimating the refraction of sound waves in upwind propagation conditions and in conditions of strong downwards refraction during near grazing propagation [34]. This is due to the fact that the high velocity gradients close to the ground lead to an overestimation of the refraction of waves and the of predicted sound pressure level.

In the present case, the source is positioned at a height of 5m above ground, which lies in the region of high wind velocity gradients. It is therefore expected that the ray code will not be capable of estimating with a detailed accuracy the variation of sound attenuation in both magnitude and phase. On the other hand, the GTPE method is not capable of taking into account accurately the effect of the wind velocity over complex terrain. As in the previous examples, two ways of calculating the effective sound speed are considered, one using only the axial component of velocity and the other using the velocity modulus. The comparison between the two methods is made using the transmission loss metric which is most suitable for consider the superposition of the contributions from the different eigenrays:

$$TL = -20 \, log \left(\frac{|p_c|}{|p_{free}|} \right) \tag{4.8}$$

where $|p_c|$ is the amplitude of the complex pressure and $|p_{free}|$ is the amplitude of the free field pressure at the distance at $1m$ from the source, e.i. $|p_{free}| = e^{ik_0}$.

In Figure 24, the predicted transmission loss using the two models is compared. It is observed that, in the flat terrain region before the hill and close to the source, the GTPE model predicts a substantial increase of TL not present in the ray theory results. The situation is reversed in the hill region and the agreement gets better at the lee side and downstream of the hill. Overall and apart from the region close to the source, the predictions of the two methods show an acceptable agreement taking into accounts their inherent limitations.

4.2 Sound propagation in turbulent atmosphere

In this section several cases of sound propagation in a turbulent atmospheric environment are studied using the turbulence model described in section 2.2. First, the calculation of the refraction index field μ through Eq. (2.61) is verified using data from the literature (Chevret et al. [35]). The following parameter values are used for the simulation:

- Correlation function: Gaussian
- Characteristic length: $L = 1\ [m]$
- Domain dimensions: $10L \times 10L = 10m \times 10m$
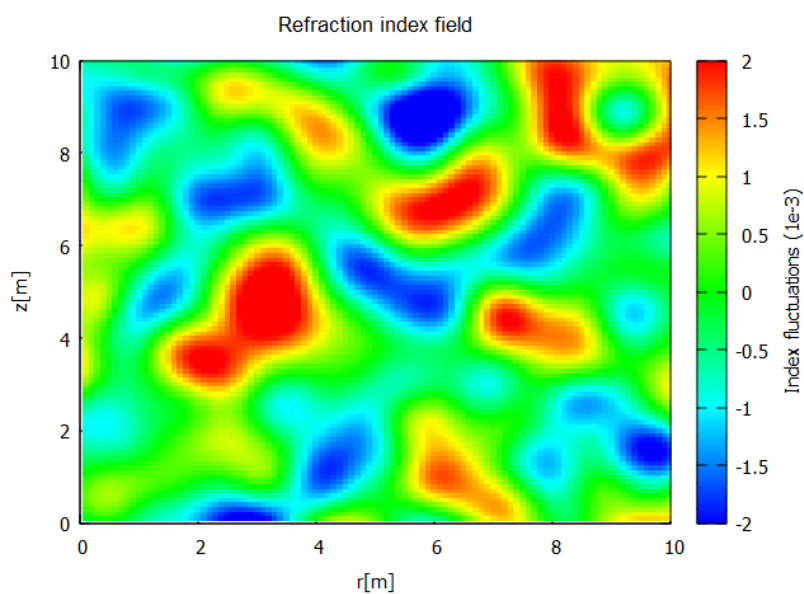- Standard deviation: $\mu^2 = 1 \cdot 10^{-6}$ (rms value of 10^{-3})
- Number of modes: 100

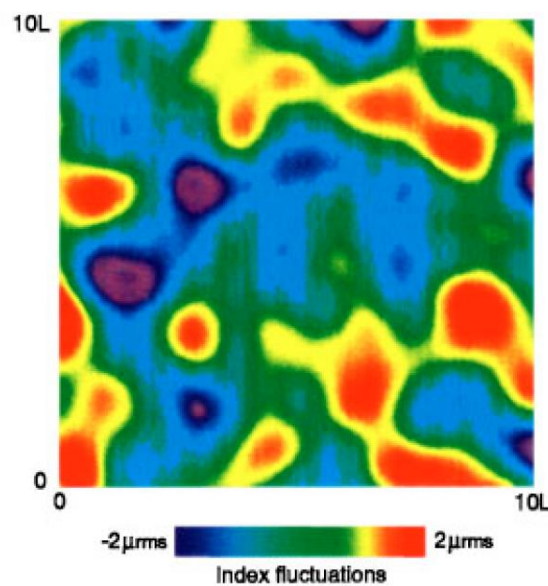Figure 25: Contours of refraction index field (μ) from the Turbulence model.

Figure 26: Refraction index field (μ) from [34].

Figures 25,26 present one random realization of the estimated contours of μ. The agreement in minimum/maximum levels as well as in the frequency of fluctuations demonstrate that the turbulence model has been well implemented. The predicted structures are of the same order of magnitude with the characteristic length $L = 1 \, [m]$ as expected.

For the next case, results for the relative sound pressure level spectrum from the developed model are compared with extensive measurements from Daigle et al. [30]. The following parameter values are used for the simulation:

- Correlation function: Gaussian
- Source position: $(r_s, z_s) = (0,1.2) \, [m]$
- Receiver position: $(r_r, z_r) = (15,1.2) \, [m]$
- Characteristic length: $L = 1.1 \, [m]$
- Standard deviation: $\mu^2 = 7.7 \cdot 10^{-6}$
- Number of modes: 150
- Number of realizations: 500
- Flow resistivity $\sigma = 10^{20} \, [Pa \cdot s/m^2] \, (rigid \, ground)$

The relative sound pressure level, ΔL, for the turbulent cases is defined as in Eq. (4.3) with $\left| p_{free} \right|$ being the amplitude of the free field pressure at distance $R = \sqrt{(z - z_s)^2 + r^2}$.

In Figure 27 the ΔL spectrum has been predicted applying the developed GTPE model with and without the turbulence model. Predictions are compared against the experimental data of Daigle et al. [30]. It is shown that compared to the non-turbulent calculation, the effect of the turbulence model is the reduction of the amplitudes of fluctuations, mainly of the attenuation maxima. This is consistent to the measurements and to the turbulent predictions (not shown here) of Chevret et al. [35].
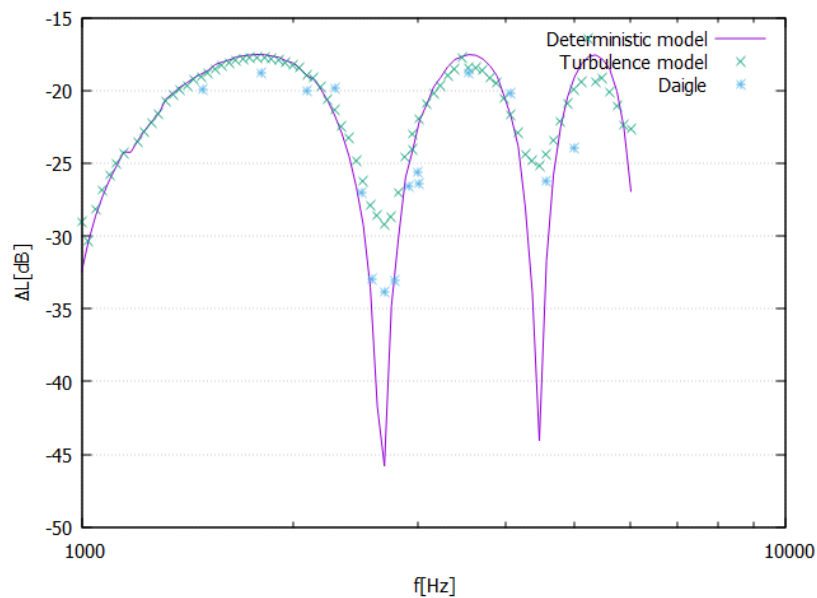

Figure 27: Relative sound pressure lever spectrum. Purple curve: Results from the deterministic (non-turbulent) model. Green points: Results from turbulence model. Light blue points: Daigle's measurements.

The second case refers to the propagation of acoustic waves in an upward refracting atmosphere. The phenomenon of the acoustic shadow zone (Fig. 6) can also occur when the sound speed gradient is negative. The paths taken by sound waves emitted from a source are curved upwards, creating a caustic that marks the boundary of the shadow zone. In this region, where a receiver is located, there are no direct sound waves originating from the source, and no sound energy can directly reach beyond the edge of the shadow zone. However, numerous outdoor experiments have shown that sound levels recorded in the shadow zone are significant. This is because sound energy manages to penetrate this area through diffraction (at low frequencies) and turbulent scattering (at high frequencies). The following parameter values are used for the simulation:

- Correlation function: Gaussian
- Characteristic length: $L = 1.1 \, [m]$
- Standard deviation: $\mu^2 = 2 \cdot 10^{-6}$
- Number of modes: 150
- Number of realizations: 50
- Source position: $(r_s, z_s) = (0, 3.7) \, [m]$
- Receiver position: $(r_r, z_r) = (0\sim1500, 1.5) \, [m]$
- Absorption layer thickness: 50λ
- Frequency $f = 424Hz \, \& \, 848Hz$
- Flow resistivity $\sigma = 3 \cdot 10^5 \, [Pa \cdot s/m^2]$

The mean sound speed profiles are given by the expression:

$$c_{eff}(\eta) = \begin{cases} c_o + a \, ln(\eta/d), & \eta \geq \eta_o \\ c_o + a \, ln(\eta_o/d), & \eta < \eta_o \end{cases} \qquad (4.9)$$

where $c_o = 340 \, m/s$, $\eta_o = 0.01m$ and $d = 6 \cdot 10^{-3}m$. The coefficient a is equal to $-0.5 \, m/s$ for a weak upward refraction and $-2 \, m/s$ for a strong upward refraction. In Figures 28-31 the predictions of ΔL using the turbulent model are compared against those from deterministic calculations (cases without turbulence) and against the experimental data of Wiener and Keast [36]. Figures 28,29 refer to the frequency of 424Hz while in Figure 30,31 the frequency is doubled to 848Hz.
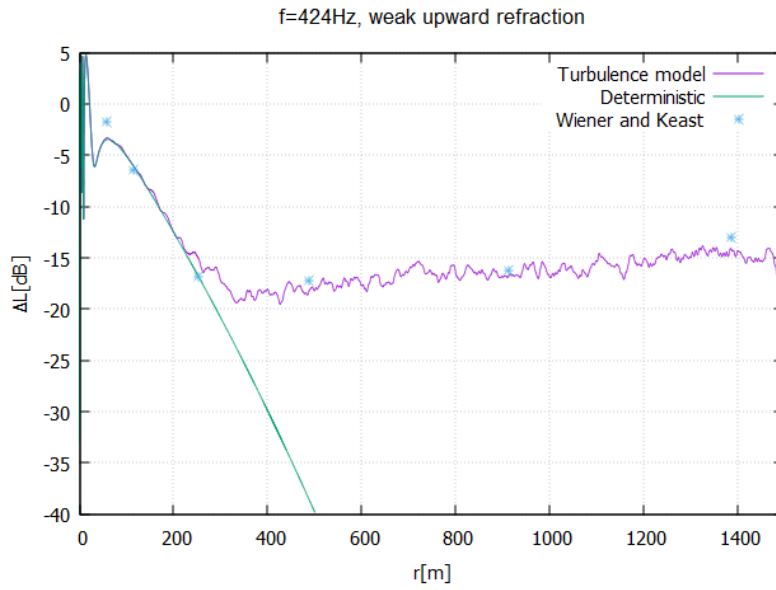
Figure 28: Predictions of relative sound pressure lever versus range under weak upward refraction at 424Hz. Purple curve: Results from the turbulence model. Green curve: Results from the deterministic (non-turbulent) model. Light blue points: Wiener's and Keast's measurements.
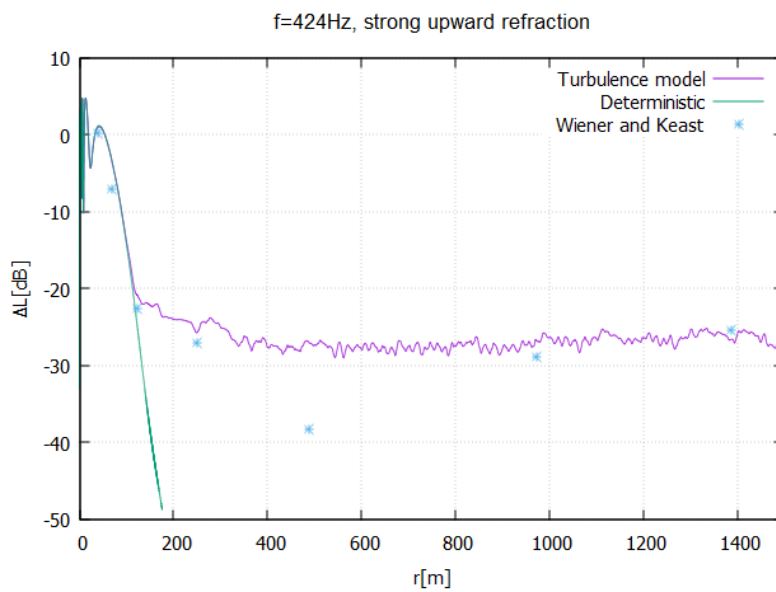

Figure 29: Predictions of relative sound pressure lever versus range under strong upward refraction at 424Hz. Purple curve: Results from the turbulence model. Green curve: Results from the deterministic (non-turbulent) model. Light blue points: Wiener's and Keast's measurements.

47

Figure 30: Predictions of relative sound pressure lever versus range under weak upward refraction at 848Hz. Purple curve: Results from the turbulence model. Green curve: Results from the deterministic (non-turbulent) model. Light blue points: Wiener's and Keast's measurements.
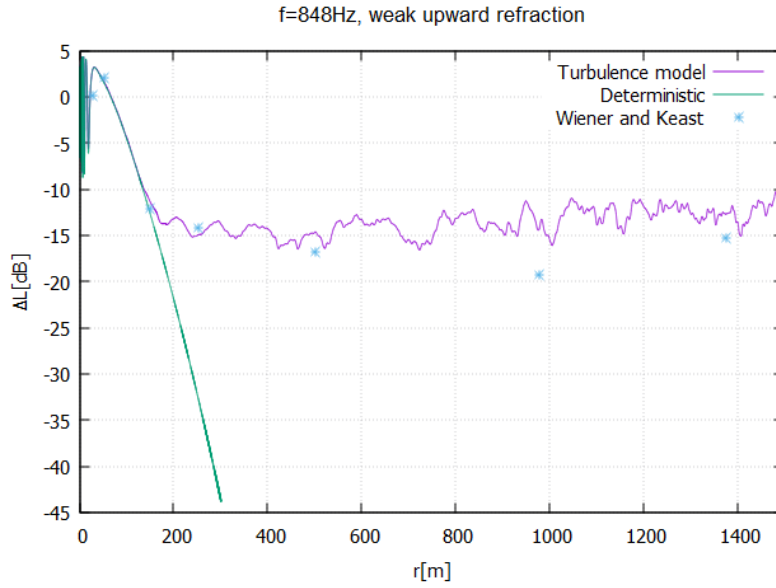

Figure 31: Predictions of relative sound pressure lever versus range under strong upward refraction at 848Hz. Purple curve: Results from the turbulence model. Green curve: Results from the deterministic (non-turbulent) model. Light blue points: Wiener's and Keast's measurements.
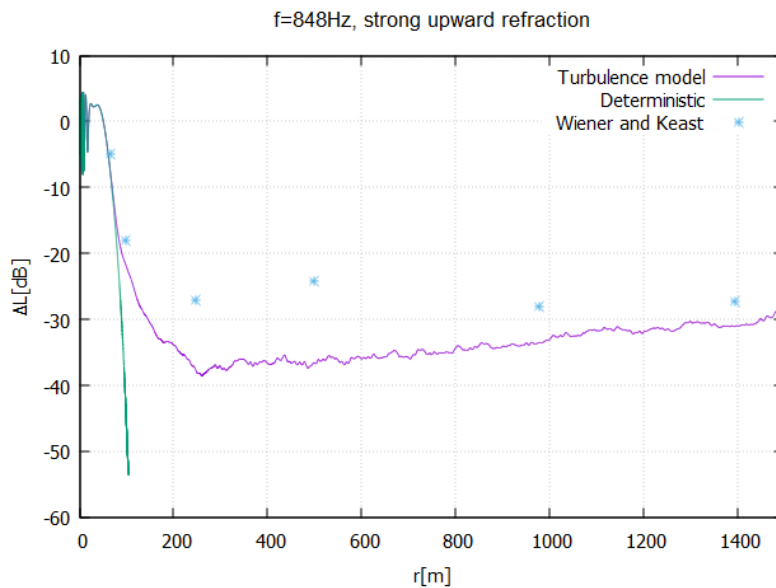
The shape of the predicted *ΔL* curve in Figures 28 to 31 exhibit strong association with the degree of upward refraction and not with frequency. The relative sound pressure level (*ΔL*) distribution over the r-range can be separated into two regions: the first extends from the source until the boundary of the shadow zone, while the second one is the area of the shadow zone. *ΔL* experience an initial steep drop which stops between the values of -15 dB to -30 dB depending on the degree of refraction. In the first region, the predictions of the turbulence and the deterministic model agree. In the second region, the predictions of the turbulence model diverge from those of the deterministic model and continue by creating a plateau with small fluctuations, which agrees with measurements. This fact can be attributed

48

to the existence of sound waves in the long-range region of an upward refracting atmosphere due to the turbulence scattering of those waves in the shadow zone.

In Figures 32 and 33 this effect is illustrated in a more detailed way, by looking at the contours of strong upwind refractive conditions. In Figure 32, the ΔL contours have been obtained using a deterministic calculation and confirm the existence of an extended shadow zone starting from the range of 200m and increasing in height with range. In Figure 33, the contours depict one turbulent realization of the ΔL field, in which it is confirmed that due to the existence of turbulence, sound waves are scattered and the extent of the shadow zone is significantly reduced compared to that predicted from the deterministic simulation.
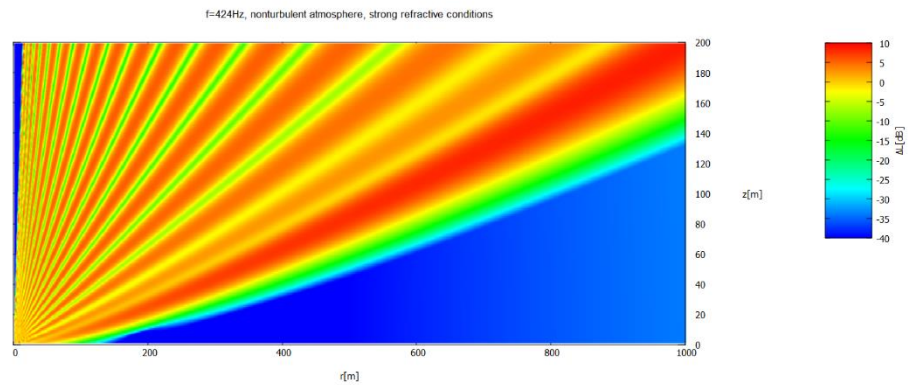

Figure 32: Contours of relative sound pressure lever under strong upward refraction and non-turbulent atmosphere at 424Hz, results from the turbulence model.
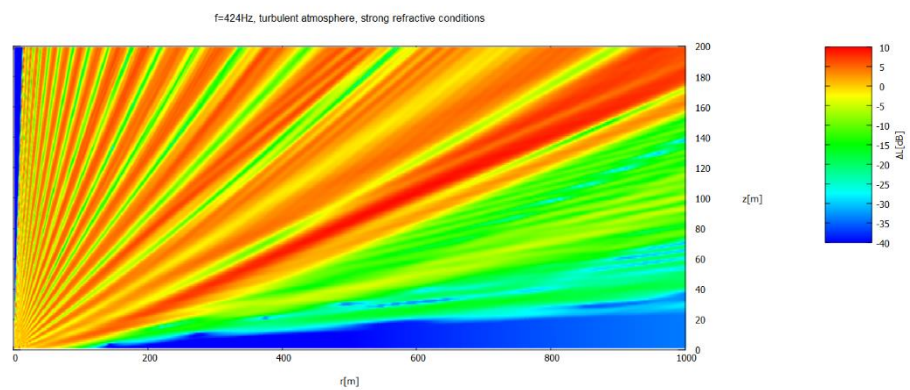

Figure 33: Contour of relative sound pressure lever under strong upward refraction and turbulent atmosphere at 424Hz, results from the turbulence model with 1 realization.

5. Conclusions and future work

5.1 Conclusions

In the present study a model capable of predicting sound propagation in the turbulent atmospheric environment over complex terrain was developed. For the case of the complex terrain, a grid transformation was incorporated, by utilizing a matrix-vector parabolic equation with elements that depend on range. The second order General Terrain Parabolic Equation (GTPE) was utilized together with second order boundary conditions in the ground and top surfaces. An absorption layer was added to the top in order to prevent reflection of acoustic waves back into the computational region. Atmospheric and spherical spreading losses were considered. Turbulence was integrated into the Parabolic Equation method with the use of the refractive-index fluctuation function, which introduced into the solution the temperature and wind velocity fluctuations that characterize the turbulent atmosphere. This was made possible through the generation of several refractive-index fluctuation realizations under the assumption of a specific spectral density for the atmospheric turbulence spectrum. The turbulent sound pressure level was predicted by performing averaging over a number of realizations.

The developed GTPE model was applied to different cases of sound propagation over irregular terrain from the literature. The results of the developed model showed good agreement with the literature predictions, with deviations attributed mainly due to different parameter values of each simulation, such as ground condition, wind velocity, grid density and source simulation. In complex terrain the assumption of a constant logarithmic profile is no longer valid. Therefore, a more realistic approach regarding the wind velocity profiles was investigated predicting the flow field with the OpenFOAM incompressible Navier-Stokes solver. In the case of a steep hill, the great acceleration of the flow at the hill top leaded to a strong refraction of sound waves downwards which increased the sound pressure level. On the other hand, when the hill was less steep, the flow experienced less acceleration and the sound pressure level decreased because it was mainly affected by the deceleration of the wind upstream and downstream of the hill.

Next, several cases of sound propagation in a turbulent atmospheric environment were studied using the developed turbulence model. First, the calculation of the refraction index field μ was verified using data from the literature. The predicted structures as well as the frequency of the fluctuations, were of the same order of magnitude as expected. Then, the relative sound pressure level spectrum was predicted applying the developed GTPE model with and without the turbulence model. Predictions were compared against the experimental data and it was shown that compared to the non-turbulent calculation, the effect of the turbulence model is the reduction of the amplitudes of fluctuations, mainly of the attenuation maxima. After that, predictions of the ΔL curve versus range were presented in cases of upward refracting atmosphere. The results exhibited the expected magnitude of sound pressure level in the acoustic shadow zone, attributed to the penetration of sound energy through the shadow zone boundary, due to turbulent scattering. A plateau with small fluctuations on the magnitude of ΔL was observed after the boundary, showing good agreement with outdoor experiments.

5.2 Future work suggestions

Potential future studies in the field of sound propagation might prioritize enhancing the turbulent GTPE model or exploring alternative numerical methods that are more intricate. Following the first direction, a more realistic representation of ground absorption could be considered, taking into account ground layers and elasticity or higher order approximation of wide-angle parabolic equation, obtained from different Padé approximations (using complex number representations) of the Helmholtz equation operator. Following the second direction, other models could be considered, such as the three-dimensional Green Function Parabolic Equation (GFPE) method or the more advanced method of solving the Linearized Euler Equations (LEE) using finite differences or finite volumes. The latter may offer more accurate and realistic simulations of sound propagation overcoming the limitations of the parabolic approximation, at the expense however of the computational requirements. In this regard, knowledge gained through the development of the turbulent GTPE model has the potential to be valuable and advantageous, by being a guideline to future research.

6. References

[1] M. Franklin, and S. Fruin, "The role of traffic noise on the association between air pollution and children's lung function," Environmental Research, 153-159, 2017.

[2] European Environment Agency Report No 22/2019

[3] M. Basner, W. Babisch, A. Davis, M. Brink, C. Clark, S. Janssen and S. Stansfeld, "Auditory and non-auditory effects of noise on health", Lancet. 2014 Apr 12;383(9925):1325-1332.

[4] Francis, Clinton & Barber, Jesse. (2013)."A framework for understanding noise impacts on wildlife: An urgent conservation priority." Frontiers in Ecology and the Environment. 11.10.1890/120183.

[5] Jens M. Hovem: "Ray Trace Modeling of Underwater Sound Propagation". August 2013. Ch.23.

[6] John M. Prospathopoulos and Spyros G. Voutsinas: "Noise Propagation Issues in Wind Energy Applications". Journal of Solar Energy Engineering, May 2005, Vol. 127, pg. 234-241.

[7] Jensen, F. B., Kuperman, W. A., Porter, M. B., & Schmidt, H.: "Computational Ocean Acoustics" (2011).

[8] John M. Prospathopoulos & Spyros G. Voutsinas: "Application of a Ray Theory Model to the Prediction of Noise Emissions from Isolated Wind Turbines and Wind Parks". Wind Energ. 2007. 10:103–119.

[9] C.L. Pekeris, Theory of propagation of explosive sound in shallow water. Geol. Soc. Am. Mem. Vol. 27 (1948).

[10] R. Raspet, S.W. Lee, E. Kuester and D.C. Chang, W.F. Richards, R. Gilbert and N. Bong: "A fast-field program for sound propagation in a layered atmosphere above an impedance ground". J. Acoust. Soc. Am., Vol. 77, No.2, February 1985.

[11] F.B. Jensen, W.A. Kuperman, M.B. Porter, and H. Schmidt, Computational Ocean Acoustics (American Institute of Physics, New York, 1994)

[12] Jensen, F. B., Kuperman, W. A., Porter, M. B., & Schmidt, H.: "Computational Ocean Acoustics" (2011).

[13] Richard Raspet, Gordon Baird and Wenliang Wu: "Normal mode solution for low frequency sound propagation in a downward refracting atmosphere above a complex impedance plane". J. Acoust. Soc. Am., Vol. 91, No.3, May 1992.

[14] J.T. Goh and H. Schmidt, A hybrid coupled wave-number integration approach to range-dependent seismo-acoustic modeling, J. Acoust. Soc. Am., 100:1409--1420, 1996

[15] R.B. Evans, A coupled mode solution for acoustic propagation in a waveguide with stepwise depth variations of a penetrable bottom. J. Acoust. Soc. Am. 74, 188–195 (1983)

[16] Erik M. Salomons: "Computational atmospheric acoustics". Springer Science and Business Media Dordrecht, 2001.

[17] Viswanathan, K., and Sankar, L. N., "Toward the Direct Calculation of Noise: Fluid/Acoustic Coupled Simulation" AIAA Journal, Vol. 33, No. 12, 1995, pp. 2271–2279.

[18] M. A. Leontovicahnd V. A. Fock, " Solution of the problem of propagation of electromagnetic waves along the earth's surface by the method of parabolic equation," J. Exp. Theor. Phys. 16(7), 557 (1946)

[19] F.D. Tappert, "The parabolic approximation method," in Wave Propagation and Underwater Acoustics, edited by J.B. Keller and J.S. Papadakis (Springer-Verlag, Berlin, 1977) p. 224-287.

[20] K.E. Gilbert and M.J. White, "Application of the parabolic equation to sound propagation in a refracting atmosphere," J. Acoust. Soc. Am. 85, 630-637 (1989).

[21] M. West, K. Gilbert, and R.A. Sack, "A tutorial on the parabolic equation (PE) model used for long range sound propagation in the atmosphere," Appl. Acoust. 37, 31-49 (1992).

[22] K.E. Gilbert and X. Di, "A fast Green's function method for one-way sound propagation in the atmosphere," J. Acoust. Soc. Am. 94, 2343-2352 (1993).

[23] Y. Delrieux and P. Malbequi, "Atmospheric sound propagation using a three-dimensional parabolic equation," Proc. Fifth Symposium on Long Range Sound Propagation, Milton Keynes, England, 147-157 (1992).

[24] R.A. Sack and M. West, "A parabolic equation for sound propagation in two dimensions over any smooth terrain profile: the Generalised Terrain Parabolic Equation (GT-PE)," Appl. Acoust. 45, 113-129 (1995).

[25] C. Kappatou, "Simulation of sound propagation in the atmosphere using the Parabolic Equation method and application to the prediction of wind turbine noise", Diploma Thesis, NTUA, Athens, October 2021

[26] R.B. Stull, An Introduction to Boundary Layer Meteorology (Kluwer, Dordrecht, 1991)

[27] V.I. Tatarski, Wave Propagation in a turbulent medium (McGraw-Hill, New York, 1961).

[28] V.I. Tatarskii, The Effects of the Turbulent Atmosphere on Wave Propagation (U.S. Department of Commerce and the National Science Foundation, Washington, D.C., by the Israel Program for Scientific translations, 1971), TT -68-50464.

[29] V.E. Ostashev, Acoustics in Moving Inhomogeneou.s Media (E&FN Spon, London, 1997).

[30] G.A. Daigle, J.E. Piercy, and T.F.W. Embleton, "Effects of atmospheric turbulence on the interference of sound waves near a hard boundary," J. Acoust. Soc. Am. 64, 622-630 (1978).

[31] K.E. Gilbert, R. Raspet, and X. Di, "Calculation of turbulence effects in an upward-refracting atmosphere," J. Acoust. Soc. Am. 87, 2428-2437 (1990).

[32] https://www.openfoam.com/

[33] Greve, Bram & Renterghem, Timothy & Botteldooren, Dick. (2005). Long range FDTD over undulating terrain.

[34] John M. Prospathopoulos & Spyros G. Voutsinas: "Determination of equivalent sound speed profiles for ray tracing in near-ground sound propagation". J. Acoust. Soc. Am., Vol. 122, No. 3, September 2007.

[35] Chevret, Patrick & Ph, & Blanc-Benon, Philippe & Juvé, Daniel. (1996). A numerical model for sound propagation through a turbulent atmosphere near the ground. The Journal of the Acoustical Society of America. 100. 3587-3599. 10.1121/1.417224.

[36] F. M. Wiener and D. N. Keast, ''Experimental study of the propagation of sound over ground,'' J. Acoust. Soc. Am. 31, 724–733 ~1959.